MEASUREMENT TECHNIQUES USED TO DETERMINE ATMOSPHERIC STRUCTURE PARAMETER

A Thesis
Presented to
The Academic Faculty

By

Cody Andrew Fernandez

In Partial Fulfillment
of the Requirements for the Degree
Master of Science in the
School of Electrical and Computer Engineering

Georgia Institute of Technology

May 2019

MEASUREMENT TECHNIQUES USED TO DETERMINE ATMOSPHERIC STRUCTURE PARAMETER

Approved by:

Dr. Gisele Bennett, Advisor
School of Electrical and Computer Engineering
Georgia Institute of Technology

Dr. David Citrin
School of Electrical and Computer Engineering
Georgia Institute of Technology

Dr. Christopher R. Valenta
School of Electrical and Computer Engineering
Georgia Tech Research Institute

Dr. Daniel LeMaster
Air Force Research Laboratory
United States Air Force

Date Approved: April 26, 2019

ACKNOWLEDGEMENTS

I am indebted to Dr. Gisele Bennett for her guidance and patience during all stages of this research. I thank Dr. David Citrin for his support in joining this thesis committee. I would also like to recognize the Georgia Tech Research Institute Electro-Optical Systems Lab for its support, and particularly Dr. Chris Valenta and John Stewart for their discussions concerning this project. I thank Dr. Michael Eismann with the United States Air Force Research Lab for his financial and technical support of this work, and particularly thank Dr. Dan LeMaster for his technical assistance. I thank U.S. Army PEO STRI and TRMC for support of the data collection which this thesis covers. Finally, I would like to thank my wife Kathleen for taking care of the children and the household during the many hours I was away completing this thesis.

TABLE OF CONTENTS

LIST OF FIGURES

SUMMARY

The objective of the proposed research is to compare and analyze the effectiveness of different atmospheric structure constant (C_n^2) measurement techniques using data collected in a field test. C_n^2 is a value used to convey the strength of optical turbulence in units of $m^{-2/3}$. C_n^2 data was collected using the following equipment: Integrated Atmospheric Characterization System (IACS), Delayed Tilt Anisoplanatism Imaging Path Atmospheric Turbulence Monitor (DELTA), Path-Resolved Optical Profiler (PROPS), a Scintec BLS-900 Large Aperture Scintillometer (LAS) and a Kipp & Zonen (K&Z) LAS system. The testing facility at Kennedy Space Center was chosen for its controlled airspace and 5km precision-leveled runway.

Optical turbulence has long plagued applications such as astronomical imaging, free space optical communication, laser-satellite communication, remote sensing, and directed energy systems. Accurate measurement of turbulence strength along a path is important for system performance for all of these applications. Each of the measurement systems in this thesis approach the measurement of C_n^2 from different fundamental principles. The scintillometers use the oldest technique and serve as verification instruments. In general, a scintillometer measures scintillations, changes in the intensity of a beam of electromagnetic energy. These changes are due to fluctuations in the refractive index of air, which randomly change the phase of the light beam as it travels across the path. Thus, the scintillometers directly measure turbulence strength averaged across a path. The scintillometer results were used as a baseline which other techniques were compared against. PROPS and DELTA use difference of differential tilt-variance (DDTV), in which the tilt-covariance of imaged light sources are measured and unique weighting functions are used to estimate C_n^2. IACS uses differential image motion (DIM) lidar, a technique in which the variance of the differential image motion of an artificial laser guidestar centroid is measured and used to estimate C_n^2.

These systems were tested during the Comprehensive Atmospheric Boundary Layer

Extinction / Turbulence Refinement Analysis EXperiment (CABLE-TRAX) from June 20-28, 2017 at the NASA Shuttle Landing Facility in Cape Canaveral, FL. CABLE-TRAX has two purposes: (1) to establish a level of confidence and performance envelopes of equipment relevant to measurement of atmospheric characteristics to be used to support High Energy Laser operations; (2) to gauge potential performance of this equipment in characterizing the atmosphere at the littoral zone. The littoral zone (land-sea boundary) has a strongly inhomogeneous atmospheric structure due to its constantly changing temperature, pressure, and wind conditions. Typical turbulence measurement instruments require a transmitter/receiver pair or transceiver pair which are difficult to set up across the littoral zone. Such double-ended equipment cannot be used to measure turbulence across a path that begins over land but terminates over a rough sea.

Overall, the measurement results show agreement of path-averaged C_n^2 usually within half an order of magnitude or less and follow similar trends across time. A trade space analysis of these systems evaluating their techniques is presented in this thesis. IACS, unlike the other devices, is able to measure across the littoral zone since it is single-ended. However the disadvantages of IACS are its size, expense, and difficulty of operation. PROPS provides a full C_n^2 profile along a path, but requires alignment and constant care unsuitable for the littoral zone. DELTA sacrifices some of the total path-profiling ability of PROPS, but is semi-single-ended and could measure across the sea with a high-contrast imaging target. The techniques compared favorably against the scintillometer results.

This thesis presents theoretical and experimental comparisons of IACS, DELTA, and PROPS, along with a system evaluation using experimental data. The analysis and results presented will be incorporated in future work developing a wave optics simulation supported by the C_n^2 measurements for slant path imaging.

CHAPTER 1
INTRODUCTION

The atmospheric structure parameter, C_n^2 , is a value used to convey the strength of optical turbulence, in units of $m^{-2/3}$. C_n^2 data was collected from different instruments during June 2017 at the NASA Shuttle Landing Facility in Cape Canaveral, FL. The data collected is from five measurement systems: (1) the Integrated Atmospheric Characterization System (IACS), (2) Delayed Tilt Anisoplanatism Imaging Path Atmospheric Turbulence Monitor (DELTA), (3) Path-Resolved Optical Profiler System (PROPS), (4) a Scintec BLS-900 Large Aperture Scintillometer (LAS), and (5) a Kipp & Zonen (K&Z) LAS. The objective of my research was to understand and compare measurement techniques used to capture the atmospheric structure parameter (C_n^2). I, in this thesis, describe the fundamental concepts and basic operation of each system, compare and analyze measurement results, and provide an overview of system performance. The results from the measurements of C_n^2 will be used in future work to compare to a computer simulation of imaging through turbulence.

The atmosphere can be considered a random medium with its randomly changing index of refraction. As light passes through the atmosphere, it is randomly perturbed due to changing conditions in temperature, wind velocity, and pressure, called atmospheric optical turbulence. Thus optical turbulence is probabilistic in nature, requiring structure functions and the atmospheric structure parameter, C_n^2, to accurately describe it. Accurate measurement and classification of optical turbulence assists applications ranging from imaging stars with telescopes to free-space optical communications. More recently, analyzing C_n^2 along a path provides efficacy estimates in Directed Energy (DE) applications. According to Gimmestad [1], range profiles are needed to support tests of laser-based military systems, analyze performance of astronomical adaptive optics systems, analyze astronomical site surveys and selection, and validate atmospheric turbulence prediction models. Adaptive

optics systems are large telescopes supplemented with wavefront sensors and a deformable mirror. The wavefront sensors measure phase errors in the input wavefront which control the deformable mirror to adjust the system for maximizing resolution of the image on the detector. Knowledge of C_n^2 and related parameters is essential for acoustic, optical, and radio propagation concerns, understanding image degradation over long paths, interpreting remote sensing observations, and evaluating adaptive optics performance [2].

The statistics and foundation of turbulence theory are attributed to Kolmogorov, Obukhov, and Corrsin [3, 4, 5]. This work was extended into wave propagation in random media by Fried, Tatarskii, and Ishimaru [6, 7, 8]. Kolmogorov classified turbulent eddies by a large outer scale, L_0, and a small inner scale, l_0. The outer scale refers to the average size of the largest eddies, ranging from a few meters just above ground to tens to hundreds of meters high above the ground. The inner scale refers to the smallest eddies, ranging from a few millimeters just above the ground to centimeters high above the ground. The difference between the inner and outer scales, the inertial subrange, is considered to be statistically homogeneous and isotropic within small regions of space. It is best represented by a structure function, rather than as a covariance [9].

The primary term used to classify turbulence strength is the refractive index structure parameter, C_n^2. Typical values for C_n^2 vary between $10^{-17} - 10^{-13} m^{-2/3}$, with smaller values at high altitudes and larger values near the ground. Stronger turbulence introduces stronger phase distortions that disrupt the optical waves passing through. This manifests in lasers through scintillation effects and beam wander [9]. In images, heavier turbulence near the camera results in more blurring, while heavier turbulence near the object results in more warping [10]. Over short time intervals at a fixed propagation distance and constant height above the the ground, C_n^2 can be approximated constant. Over longer distances and slant paths it varies with propagation distance, indicated as $C_n^2(z)$ [9].

The time-varying properties of turbulence can be largely ignored with some simplifying assumptions. Over short time intervals (100 μs or less), time dependence can be removed

from the refractive index, since the speed of light is much faster than the rate at which the properties of turbulent eddies change. Kolmogorov turbulence theory states that turbulence remains mostly constant across small distances within the inner (l_0) and outer (L_0) scales of turbulence. Additionally, one can invoke the Taylor frozen-flow hypothesis, in which turbulent eddies are treated as frozen in space and blown across the optic axis by the mean wind velocity [11].

Measurement of turbulence strength is a challenging problem. I evaluate the performance of DELTA, PROPS, and IACS for measuring C_n^2 by comparing data collected from the field test as described in Chapter 4.

CHAPTER 2

BACKGROUND

This section introduces some of the fundamental science used in the systems discussed in later chapters. Important terms and concepts from atmospheric optical turbulence are presented. Current turbulence measurement techniques, the systems which employ these techniques, and their shortcomings are also introduced.

2.1 Atmospheric Optical Turbulence

Optical turbulence is the term used to describe the atmosphere's randomly changing refractive index. The diurnal heating and cooling of the Earth's surface by the sun causes a large-scale temperature differential across the atmosphere, resulting in wind. Wind can be divided into laminar flow and turbulent flow. Smaller scale local temperature differences mixed by this turbulent flow result in turbulent eddies. These turbulent eddies have randomly changing refractive indices due to their varying size, shape, temperature, and density. They are defined by an inner scale l_0, on the order of millimeters to centimeters, and an outer scale L_0 on the order of tens to hundreds of meters. The distance between the inner and outer scales is called the inertial subrange [9].

Index of refraction at a point $\mathbf{R}$ in space and time t is [9]

$$n(\mathbf{R}, t) = \langle n(\mathbf{R}, t) \rangle + n_1(\mathbf{R}, t). \tag{2.1}$$

Let $\langle n(\mathbf{R}, t) \rangle = n_0 \cong 1$ be the mean value of the refractive index and $n_1(\mathbf{R}, t)$ be the random deviation of the refractive index from the mean. Thus $\langle n_1(\mathbf{R}, t) \rangle = 0$. Normalizing Equation 2.1 by n_0 produces

$$n(\mathbf{R}) = 1 + n_1(\mathbf{R}). \tag{2.2}$$

Thus $n_1(\mathbf{R}) = n(\mathbf{R}) - 1$ can be considered a measure of the deviation of the refractive index from its free space value, where $n_1(\mathbf{R})$ is time-averaged and distinct from $n_1(\mathbf{R}, t)$[12]. From this, index of refraction at optical and infrared wavelengths can be written as [13]

$$n - 1 = a_d(\lambda)P_d/T + a_w(\lambda)P_w/T, \tag{2.3}$$

where $a_d(\lambda)$ and P_d are the wavelength-dependence function and partial pressure of the dry air in mbar, $a_w(\lambda)$ and P_w are the wavelength dependence function and partial pressure of water vapor in mbar, and T is temperature in Kelvin. The wavelength-dependence functions are defined in [14]. In the vast majority of turbulence applications, the dry-air term dominates. Since C_n^2 varies by more than an order of magnitude, it is customary to drop the wavelength dependence in Equation 2.3 and solve the dry-air wavelength dependence function at $\lambda = 0.5\mu$m, resulting in

$$n(\mathbf{R}) - 1 = 79 \times 10^{-6} \frac{P(\mathbf{R})}{T(\mathbf{R})}, \tag{2.4}$$

where $P(\mathbf{R}) = P_d + P_w$. Seeing that refractive index is unitless, the units of 79×10^{-6} are K/mbar. Because $\langle n_1(\mathbf{R}) \rangle = 0$, the covariance function of $n(\mathbf{R})$ is [9]

$$B_n(\mathbf{R_1}, \mathbf{R_2}) \equiv B_n(\mathbf{R_1}, \mathbf{R_1} + \mathbf{R}) = \langle n_1(\mathbf{R}) n_1(\mathbf{R_1} + \mathbf{R}) \rangle. \tag{2.5}$$

For statistically homogeneous and isotropic random fields, the covariance function reduces to $R = |\mathbf{R_1} - \mathbf{R_2}|^2$. Thus within the inertial subrange, the refractive index structure function can be expressed as [9]

$$D_n(R) = 2[B_n(0) - B_n(R)] = C_n^2 R^{2/3}, \tag{2.6}$$

where the structure function follows the two-thirds power law. Beland [14] shows that C_n^2

can be represented as

$$C_n^2 = (\delta n/\delta T)^2 C_T^2 = [(n-1)/T]^2 C_T^2, \tag{2.7}$$

where C_T^2 is the temperature structure parameter defined as [15]

$$C_T^2 = \langle (T_2 - T_1)^2 / R^{2/3} \rangle_{av} = D_T / R^{2/3}, \tag{2.8}$$

where D_T is the temperature structure function and C_T^2 is independent of R. The temperature structure function is the ensemble average of two different temperatures (T_1 and T_2) separated by a distance R and following the two-thirds power law. These equations hold because of the statistically homogeneous and isotropic nature of turbulence in the inertial subrange. Equation 2.4 can be substituted into Equation 2.7 producing

$$C_n^2 = \left(79 \times 10^{-6} \frac{P}{T^2}\right)^2 C_T^2, \tag{2.9}$$

where C_n^2 has units of $m^{-2/3}$. Equation 2.9 is a common expression for C_n^2 seen throughout the literature. This treatment is accurate for the Planetary Boundary Layer (the layer closest to the ground). Turbulence strength decreases as distance from Earth increases. As such, the Hubble space telescope does not suffer the effects of atmospheric optical turbulence. Additionally, turbulence closer to the aperture of an imaging system causes more distortion versus turbulence closer to the target (as seen in telescope imaging versus remote sensing). Finally, C_n^2 can vary across a path of length z, becoming $C_n^2(z)$. The primary measure of comparison used in this thesis is path-averaged C_n^2, where measurements produce a C_n^2 value that is averaged across the path of the measurements. The units of path-averaged C_n^2 are still $m^{-2/3}$. This is not to be confused with path-integrated C_n^2, in which $C_n^2(z)$ is integrated across the length z of the path producing units of $m^{+1/3}$.

2.2 METAR

The Aviation Routine Weather Report (METAR) [16] is the name of the international meteorological code for aviation routine weather reports. Air Traffic Control (ATC) towers provide hourly METAR updates from measurements and observations conducted at the ATC tower. METAR provides information vital to airmen about atmospheric conditions such as wind speed and direction, visibility, sky cover (such as cloud density), temperature and dew point temperature, and pressure. The dew point temperature is the temperature at which a parcel of air would condense into water (or dew). The dewpoint spread is simply the difference of an air parcel's temperature and its dewpoint. As the dewpoint spread decreases to zero, the relative humidity of the parcel increases to 100% and the parcel becomes saturated. C_n^2 measurements can be immediately affected by changes in wind speed/direction and dew point spread. This can be seen in Equation 2.9, where changes in pressure and temperature directly affect C_n^2.

Local winds can also affect turbulence. Local winds develop and flow in the direction of a pressure-gradient force, which is a force created by a difference in pressure and which travels from high to low pressure. Also present is the frictional force developed by the terrain opposing the force of wind flowing across it. The conditions of temperature, dewpoint, and wind combine to either strengthen or weaken measured C_n^2. Though METAR data does not directly provide C_n^2 measurements, it can be used to give insight into potential C_n^2 anomalies as demonstrated in Chapter 5.

2.3 Measurement Techniques

Lawrence et al. [15] understood that large-scale meteorological variables such a temperature gradient and wind velocity were insufficient to determine the properties of turbulence. Variation of the refractive index of air is due to the variation of the density of air, which is in turn caused by the variation of the temperature of air. They used a pair of fine platinum

wires as resistance thermometers to directly measure the temperature structure parameter C_T^2 seen in Equation 2.8 and converting it to C_n^2 using Equation 2.9. These temperature probes were separated by distances on the order of centimeters (bounds of 1 mm to 1 m) and time-averaged to produce a point measurement of C_n^2. This aligns with the inner scale l_0 of turbulence. The probes were also fixed to an aircraft and used to produce a rough vertical profile of C_n^2. The authors then set out to correct the saturation of scintillometers by strong turbulence by extending Tatarskii's saturation theory enhanced by the measurements the temperature probes provided [17]. They found that scintillometers of the time mismeasured C_n^2 at distances exceeding 1000 m due to super-saturation of the observed scintillations. The advantage of using pairs of sensors is that the structure-function measurement acts as a spatial filter, discriminating against irregularities with scales larger than R, giving insight in to the spatial distribution of C_n^2. It will be different even with the same temperature around R. The correlation of samples taken in adjacent measurement cells is shown in Figure 4 of [15] which displays measurements of probes at 2m above ground with spacings of 1, 3, and 10cm. The authors apply a 1-hr smoothing average, so the measurements are all within an order of magnitude but still differ. They later developed a scintillometer measurement technique [18] that avoided the effects of inner scale l_0 and produced saturation-resistant measurements of C_n^2 by using large incoherent transmit and receive apertures. Throughout the paper they detail the different ways the path-weighting function of their scintillometer was affected by receiver aperture size, inner scale, variance of log-amplitude variance, and detector count. These scintillometer and temperature-based techniques form the groundwork of current turbulence measurement systems.

Eaton [2] describes a variety of modern techniques (scintillometers, Differential Image Motion Monitor (DIMM) systems, RADAR sensing, SOnic Detection and Ranging (SODAR) sensing, balloon rings, kite/tethered blimps, path-profilers, and Differential Image Motion (DIM) lidar) for measuring parameters of importance to atmospheric optical turbulence. The pressing need of modern techniques is to provide range-resolved turbulence

profiles for vertical, horizontal, and slant paths.

DIMM systems directly measure the transverse coherence diameter r_0. r_0 for a plane wave is related to C_n^2 by [19]

$$r_0 = [0.42k^2 \cos^{-1}(a) \int_0^Z C_n^2(z)dz]^{-3/5}, \tag{2.10}$$

where $k = 2\pi/\lambda$ is the wavenumber, a is the zenith angle, and Z is distance in meters. DIMM systems calculate r_0 from image motion, eliminating other sources of error by using multiple apertures and source beams. Sarazin and Roddier [20] demonstrated a successful technique for finding DIM variance that later inspired the IACS method. Instead of the refractive index structure function, it uses the covariance of angle-of-arrival fluctuations of DIM over a distance d

$$\sigma^2(d) = 2[B(0) - B(d)], \tag{2.11}$$

where $B(d)$ is the covariance of angle-of-arrival fluctuations defined as

$$B_\alpha(\xi, \eta) = \langle \alpha(x, y), \alpha(x - \xi, y - \eta) \rangle. \tag{2.12}$$

This covariance must be solved for image motion in the longitudinal and transverse directions of the image plane. Holding $\eta = 0$ and $\xi = d$ where d is the aperture separation, Sarazin and Roddier show [20] under Kolmogorov turbulence conditions that the longitudinal covariance is

$$B_l(d) = 0.097 \left(\frac{\lambda}{r_0}\right)^{5/3} \left(\frac{\lambda}{d}\right)^{1/3}. \tag{2.13}$$

Similarly holding $\xi = 0$ and $\eta = d$ produces

$$B_l(d) = 0.145 \left(\frac{\lambda}{r_0}\right)^{5/3} \left(\frac{\lambda}{d}\right)^{1/3}. \tag{2.14}$$

Figure 2.1: Modern DIMM system with four apertures [2].

and setting both $\eta = 0$ and $\xi = 0$ results in

$$B_\alpha(0,0) = 0.179 \left(\frac{\lambda}{r_0}\right)^{5/3} \left(\frac{\lambda}{D}\right)^{1/3}, \tag{2.15}$$

where D is the diameter of the apertures. These expressions can be plugged into Equation 2.11 to solve for DIM variance in the longitudinal and transverse directions. Figure 2.1 shows a modern four-aperture DIMM system, much smaller and lighter than its predecessors [2]. Each aperture is used to separately determine the centroid of the reference star, and image variances of each centroid are captured for each aperture. The total variance of these separate centroid variances is then measured and used to calculate r_0. In this way, errors due to tracking, vibration, and wind loading are ignored since they display in all four apertures and get subtracted out.

Doppler radars can be calibrated to measure C_n^2. Radar systems operate in all weather and provide long-term continuous data at high temporal and spatial resolutions over a variety of altitude ranges of interest. One example of an FMCW radar [21] operates at

2.9GHz($\pm$)100MHz, is sensitive to -165DBm, and has high spatial and temporal resolution (2-m range and 12s). These systems are so sensitive they have revealed new features in the atmosphere, and their high resolution can even reveal insects. Unfortunately they are large (two 10-foot diameter parabolic antennas mounted side-by-side on a steerable mount), but are portable with some effort. Conversely, a stationary 50MHz radar sports an antenna 500ft in diameter with a power aperture product of $10^8 W m^2$. It provides a profile every 3 minutes at 150m height resolution from 2-20km above ground level. A 50MHz radar used at White Sands Missile Range took data in this manner for 6 years, and this data used to study long-term turbulence effects such as persistent C_n^2 layers, eddy dissipation rates, and the interaction of turbulence and gravity waves [22, 23, 24].

SODAR sensing has traditionally been used to determine wind profiles. However, a carefully calibrated system that accounts for attenuation can provide profiles of C_T^2 from which C_n^2 can be determined if extra measurements of air temperature, humidity, and pressure are taken [25]. Sodars are transportable, relatively low cost (at least compared to radar), and directly sense a parameter of interest C_T^2, but have limited range due to the high attenuation in the acoustic range and contamination from external noise sources.

Balloon rings use fast response sensors mounted on packages similar to radiosondes. They must account for wake effects (wake contamination) due to the warming and cooling of the balloon throughout the day. A balloon-ring platform [26] that avoids wake contamination uses a balloon that is actually an inflatable polyethylene tube with a pressure relief valve and a ring that is actually an approximately 30-foot diameter octagon suspended just beneath the balloon. Fine-wire sensors ($1 \mu m$ diameter) mounted at various separations on a boom tangential to the "ring" measure temperature and velocity fluctuations.

A kite/tethered blimp can be used to estimate C_T^2 and C_n^2 via wire sensors for sensing temperature and velocity fluctuations. Single fine wires are always directed into the wind via a vane. A new version [27] can measure 3-D winds with added sensor packages including accelerometers, GPS, thermocouples, and a three-axis sonic anemometer

providing measurements of fluctuations in temperature which can give C_T^2. The system is mounted to a kite during high-wind or a blimp during low-wind conditions. Both kite and blimp models are tethered to a winch on a truck, where an electromagnetic particle clutch maintains constant capstan speed even as the diameter of line on the take-up spool changes. These measurements are point measurements useful for verification but cannot provide a path-profile.

A precursor to the PROPS system, the original path-profiler used differential-tilt measurements to arrive at statistics with unique weighting functions over a propagation path [28]. The unique functions derived a reconstructor matrix used to determine C_n^2 profiles. In this early setup, two telescopes are placed opposite each other across a path, each imaging 3 wavelengths of lasers onto 3 pairs of apertures. Filters put the desired wavelength on each subaperture and calculate C_n^2.

The precursor to IACS was the brassboard DIM lidar [1]. Similar to a DIM monitor, it calculates the differential image motion of a source. Its source is a lidar-generated artificial guide star focused at various distances, with the imaging system range-gated to the specified distance. These DIM variance measurements are then applied to an inversion matrix algorithm which provides C_n^2 profile information.

Though the radar, sodar, balloon ring, and kite/blimp systems provide measurements or vertical profiles that help determine C_n^2, they don't provide data specific enough to a directed energy (DE) application, for estimating turbulence strength across a varying path like the littoral zone. Thus the path-profiler systems (DELTA and PROPS) and the DIM lidar (IACS) aim to fill that gap by providing a profile of C_n^2 values along a path. Determining turbulence strength along the path informs a DE system operator of the likelihood that the directed energy will reach its target in spite of the deleterious effects of turbulence. A portable, direction-agnostic single-ended path-profiler would be the most desirable turbulence measurement system.

CHAPTER 3

THEORY AND OPERATION OF EACH SYSTEM

This section focuses on the underlying theory and operating principles of the C_n^2 measurement systems analyzed for this thesis. This is an extension of the background, providing a more focused overview of the science and engineering behind these systems. In short, scintillometers measure C_n^2 directly based on scintillation theory, Path-Resolved Optical Profiler System (PROPS) and Delayed Tilt Anisoplanatism Imaging Path Atmospheric Turbulence Monitor (DELTA) use difference of differential tilt variance (DDTV) based on tilt covariance measurements of a source, and the Integrated Atmospheric Characterization System (IACS) Optical Turbulence Profiler (OTP) uses a technique referred to as Differential Image Motion (DIM) lidar, measuring the DIM variance of an imaged laser guidestar. Each of these systems will be described in this chapter.

3.1 Scintillometer

A scintillometer consists of a transmitter unit which emits an electromagnetic beam into a receiver unit, typically across a horizontal path. The receiver unit of the Kipp & Zonen (K&Z) Large Aperture Scintillometer (LAS) is shown in Figure 3.1. Not shown is an identically-appearing transmitter unit 1.5km away. In general, scintillometers measure scintillations, changes in the intensity of the beam of light. These changes are due to fluctuations in the refractive index of air which randomly change the phase of the light beam as it travels across the path. Refractive index changes can be further broken down into changes due to temperature, humidity, pressure, and the covariance terms connecting them [29]. A classic tool in atmospheric optics, scintillometers are notorious for never measuring exactly the same C_n^2 value. Due to the probabilistic nature of refractive index changes and the drawbacks of intensity-based measurements, two scintillometers set next to each other

may not report the same exact magnitude of C_n^2 measurement. The most important element of comparison is that both units show the same trends in path-averaged C_n^2 over time. Despite these magnitude discrepancies, scintillometers are still considered the measurement baseline, and accuracy of new techniques is often determined by comparing their outputs to scintillometer data.

3.1.1 Inputs, Processing, and Outputs

The K&Z LAS uses a near-infrared beam to measure intensity fluctuations. Specifically, it uses the measured variance of intensity fluctuations to directly calculate C_n^2,

$$C_n^2 = 1.12\sigma_{lnI}^2 D^{7/3} L^{-3}, \tag{3.1}$$

where σ_{lnI}^2 is the measured variance of the natural logarithm of intensity fluctuations, D is the aperture diameter, and L is the path length [30]. The time scale over which the variance of the natural logarithm (also known as the log-amplitude variance) is measured is not mentioned. Equation 24 of [18] shows conditions in which fractional irradiance could be used instead of log-amplitude variance. As for the breakdown of intensity fluctuations, pressure can be neglected, leaving the structure functions for temperature (C_T^2) and humidity (C_Q^2) and a covariance term (C_{TQ}). It can be shown [30] that humidity related contributions are much smaller than those of temperature, and thus the LAS is sensitive primarily to intensity fluctuations caused by changes in temperature.

It is also important to understand how the path-weighting function of the LAS influences the measurements it produces. This weighting function arises as a result of the first-order scattering theory illumined by Tatarskii [7]. The K&Z LAS uses same-sized apertures for the transmitter and receiver. When it measures intensity fluctuations across the path, it gives some measurements more significance than others. This is shown in Figure 3.2. This Gaussian-shaped curve favors measurements taken in the middle of the path

Figure 3.1: The receiver unit of the K&Z LAS.

and zero-weights measurements at the transmitter and at the receiver. This means that any fluctuations present at either end of the path are not taken into consideration. This could lead to inaccurate measurements if a strong pocket of turbulence directly in front of the transmitter or receiver is not added into the averaging of the measurements.

For the K&Z LAS, intensity fluctuations are recorded and output as a voltage. This voltage V is easily input into

$$C_n^2 = 10^{(V-12)} \tag{3.2}$$

to determine path-averaged C_n^2 [30]. Equation 3.2 is for the use of an operator, whereas Equation 3.1 addresses the underlying physics of the system. The -12 term in the exponent corresponds to the typical voltage output of the system ($-5V$ to $0V$) resulting in C_n^2 measurements of 10^{-17} to 10^{-12}.

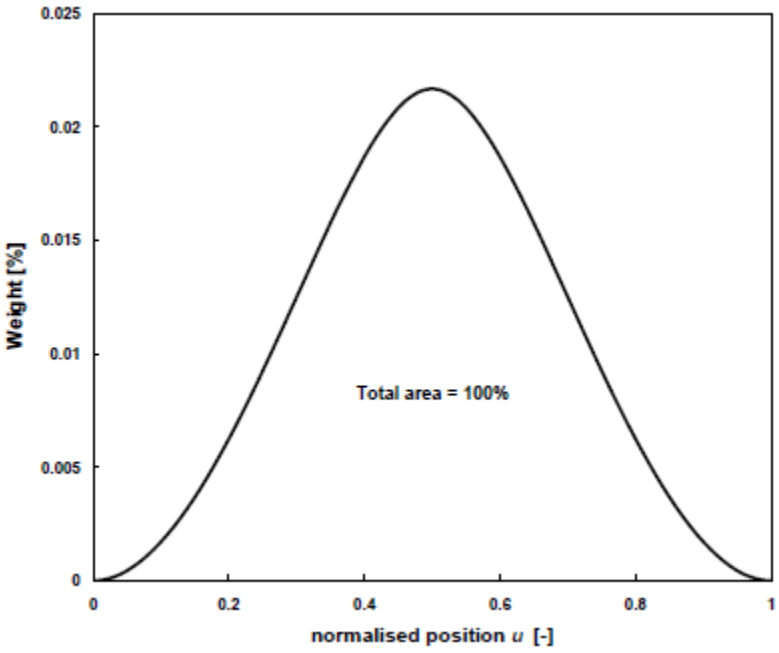

Figure 3.2: The path-weighting function of the K&Z LAS [30].

3.2 Difference of Differential Tilt Variance (DDTV) Systems

PROPS and DELTA measure difference of differential tilt variance (DDTV) based on papers by Whiteley [28, 31]. DDTV measures a phase-related quantity, rather than an irradiance-related quantity like a scintillometer. This leads to several advantages of DDTV, including insensitivity to noise due to gimbal motion, additive detector noise, and outer scale of turbulence and immunity to scintillation saturation effects. However, it still produces lower resolution C_n^2 profiles than the profiles produced by the radar systems described in Chapter 2.

DDTV labeled σ_δ^2 is strictly defined as [31]

$$\sigma_\delta^2 \equiv \langle (d_{1p} - d_{2p})^2 \rangle - \langle (d_{1s} - d_{2s})^2 \rangle, \tag{3.3}$$

where d_{1p}, d_{2p} are the primary differential-tilt variances and d_{1s}, d_{2s} are the secondary differential tilt variances. Primary and secondary variances correspond to the designated aper-

tures receiving the centroid measurements. It can be shown [31] that Equation 3.3 reduces to

$$\sigma_\delta^2 = 2(\langle t_{1s} t_{2s} \rangle - \langle t_{1p} t_{2p} \rangle), \tag{3.4}$$

where $t_{1p}, t_{2p}, t_{1s}, t_{2s}$ are the primary and secondary tilt covariances of the measurements the apertures receive. From this, Whiteley shows that tilt covariances can be converted into weighted integrals of C_n^2 which are normalized across the propagation path [31].

An *M*-length vector of measurements is collected. By partitioning the propagation path into *N* partitions of nearly-uniform turbulence strength, an *MxN* matrix **P** of weighting functions can be determined, and an *N*-length vector of C_n^2 values can be separated from it [31],

$$\mathbf{m} = \mathbf{P}\mathbf{c}. \tag{3.5}$$

Solving for **c** should be as simple as left-multiplying **m** by $\mathbf{P^{-1}}$, but **P** is rarely invertible. The pseudo-inverse of **P**, designated **H**, is instead multiplied by **m** to obtain $\hat{\mathbf{c}}$, the least-squares estimate of **c**.

The weighting functions in $\hat{\mathbf{c}}$ are developed differently from those previously seen in the scintillometer, which is symmetric about the midpoint of the propagation path and 0 at both ends of the path. DTV is always zero-weighted at the source plane and max weighted at the aperture plane (receiving end) for non-converging geometry. By taking the difference of DTV at the aperture plane for converging and non-converging geometries the aperture plane weighting can be removed. This gives DDTV an adjustable weighting function that is zero at both ends but peaks somewhere along the path. Placing apertures close together pulls the peak of the weighting function closer to aperture plane. Moving sources closer together pushes the peak closer to the source plane. In general, the optimum weighting function corresponds to the biggest Fresnel number of apertures which provides maximum sensitivity.

3.2.1 PROPS: Inputs, Processing, and Outputs

PROPS is a direct application of the DDTV theory. Figure 3.3 diagrammatically shows the PROPS data collection process. A single unit has two apertures which collect an ensemble of spot centroid measurements of three different wavelength sources (red, green, blue) across a propagation path using a primary and secondary geometry on the focal plane of its imaging camera (a wavefront sensor assembly). The wavefront sensor directly measures the local tilt of the incoming wavefront using an array of small lenslets. These measurements are processed into a collection of DDTV quantities. DDTV quantities are selected from the ensemble of measurements based on the uniqueness of their corresponding theoretical path-weighting functions. Measurements that do not correspond to a unique theoretical path-weighting function are discarded. Prior knowledge of these unique path-weighting functions allows for the creation of a reconstructor matrix $\mathbf{H}$. An estimate of turbulence along the path $\hat{\mathbf{c}}$ is produced from applying $\mathbf{H}$ to the collected measurements $\mathbf{m}$. Additionally, the PROPS units record the deviation of each source and its intensity fluctuation. These results (along with the turbulence estimates) are processed and communicated across devices via a built-in wireless link. PROPS can detect changes in turbulence along a path resulting from the surface features along that path. It can also estimate cross-wind speeds as seen from both sides of the path. A single PROPS unit is shown in Figure 3.4.

3.2.2 DELTA: Inputs, Processing, and Outputs

DELTA is another class of DDTV system that images a scene with high-contrast, trackable features with a typical camera, rather than a wavefront sensor. This means DELTA must use image processing techniques rather than directly measuring the wavefront tilts. It measures the differential jitter of feature pairs as a function of angular separation. This differential jitter can be considered the tilt covariance and processed using the DDTV techniques as explained previously. DELTA is unique in that it is single-ended. This comes with the downside that its path-weighting functions are the ones proposed by the original

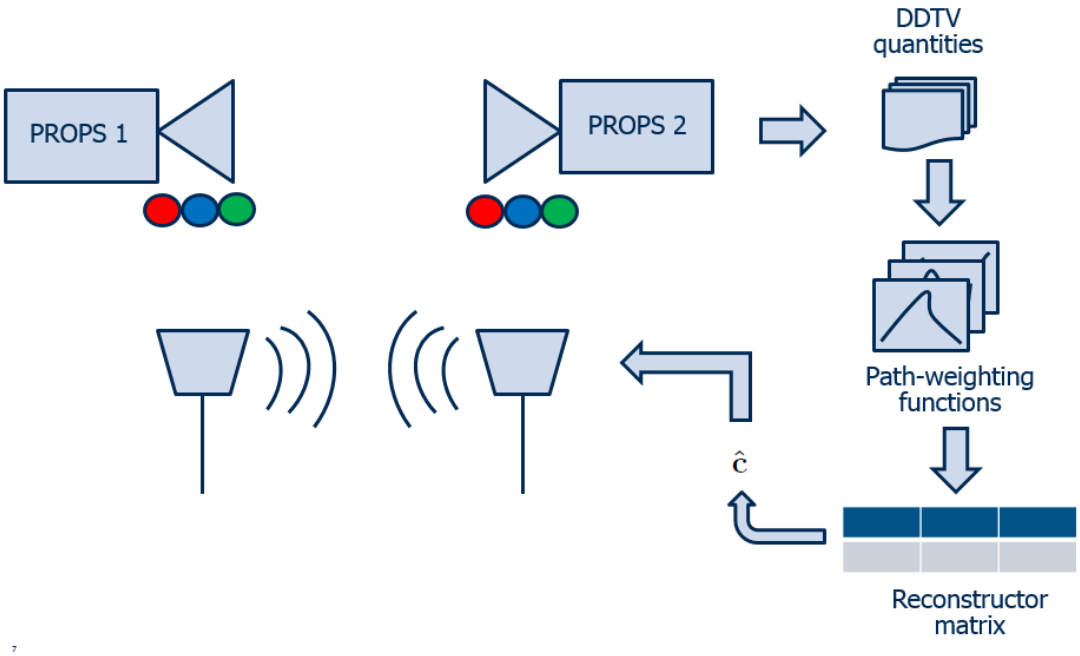

Figure 3.3: Illustration of the PROPS data collection process.

Figure 3.4: The PROPS unit.

Figure 3.5: The DELTA imaging unit.

DDTV method, without the corrections that come from the extra equipment of PROPS. DELTA measurements are separated into ten bins. Path-weighting functions in each bin are heavily weighted at the receiver, extending to the midpoint of the path, but effectively zero at the target. Thus, similar to the scintillometer, any turbulent effects at the target are underreported in its estimation. This could lead to underestimates of C_n^2. A single DELTA imaging unit consisting of a telescope, tripod, camera, and computer is shown in Figure 3.5.

3.3 Differential Image Motion (DIM) Systems

IACS OTP is based on Differential Image Motion Monitors (DIMM) which view natural stars through two or more spatially separated apertures and acquire a series of images of the stars. IACS OTP uses a technique called DIM lidar (laser radar) to measure the DIM variance between pairs of artificial guidestars. First, a laser beam is focused at a defined

distance. The light from this laser scatters off a scattering volume and is received by a telescope with two spatially separated subapertures. A glass wedge separates the two images in the focal plane. Differential motion between the images is then measured in the conventional way as detailed by Sarazin [20] and highlighted in Chapter 2.3, which involves determining the centroid of each imaged star, calculating the separate variances of the centroid, then calculating the mutual variance of the centroid variances. Equipped with this DIM variance, C_n^2 can be estimated along the defined distance. By firing the laser at subsequently increasing ranges, path-averaged C_n^2 can be determined along a path of increasing length. This allows for the derivation of a range profile, i.e. a profile of the strength and behavior of turbulence across the path [1].

The DIM lidar technique brings with it many important advantages. For one, it measures the differential motion of images and not their sizes. This means it is fundamentally immune to any effects that cause image blurring, vibration, laser instability, diffraction of the transmitting and receiving apertures, environmental changes in the system modulation transfer function, and aerosol image blur. Additionally, the scattering volume is generally an incoherent source and thus less sensitive to laser speckles and scintillation than a conventional DIMM. DIM lidar is not affected by beam reciprocity, making it insensitive to variations of outer scale (L_0). Like PROPS and DELTA, IACS OTP measures a phase related phenomenon, so it does not saturate with increasing range and turbulence intensity. Finally, since it is based on direct detection rather than coherent detection, it can be built from commercial off-the-shelf parts, and the optical assembly doesn't need extreme stability [1].

3.3.1 IACS OTP: Inputs, Processing, and Outputs

IACS was designed to characterize optical propagation paths during outdoor tests of electro-optical systems. It uses three lidars to achieve this: a 355nm imaging lidar known as the Optical Turbulence Profiler (OTP), a 355 nm Raman lidar for profiling water vapor, and

Figure 3.6: IACS optical shelter, control shelter, and power supply.

an aerosol lidar operating at 355, 1064 and 1627 nm. All the lidars with their transmit and receive optics are on a common mount that can rotate from 10° below horizontal to the vertical (90° above the horizontal) [32]. The system is divided into two shipping containers, shown in Figure 3.6. The lidar mount, laser subsystem, and some of their controls comprise the first box, while the second box serves as the true control center housing computers, personnel, and HVAC units. A close-up of the optics system is shown in Figure 3.7

Though IACS is used to fully characterize atmospheric conditions to include aerosols and a water vapor profile, this thesis focuses on the OTP subsystem. IACS OTP uses a 354.7 nm UV laser because this wavelength generates the largest Rayleigh backscattered signal in clear air and because commercial lasers with large pulse energies are available at this wavelength [32]. IACS OTP calculates DIM variance from a series of guide star centroids from successive pulsed laser shots. Sarazin [20] and Eaton [33] separately determined that

Figure 3.7: Detail of IACS optics mount.

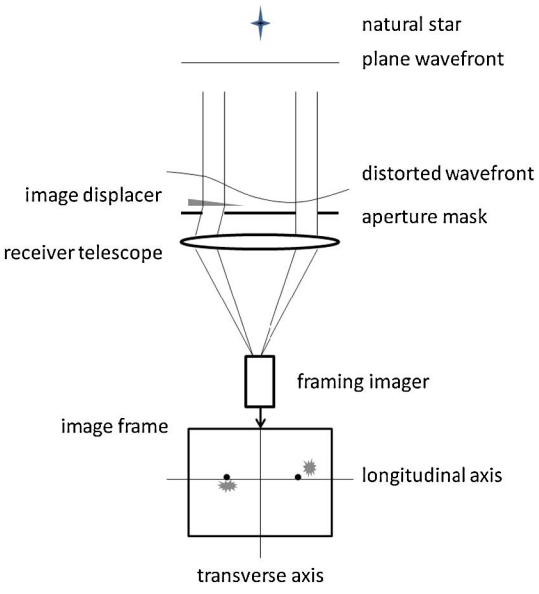

Figure 3.8: The Differential Image Motion Monitor imaging process [19].

DIM variance (units $radians^2$) takes the form

$$\sigma^2_{DIM} = f(d/D)D^{-1/3}\hat{C}^2_n, \tag{3.6}$$

where f is a function, D is the subaperture diameter (units m), d is the subaperture separation (units m), and $\hat{C}^2_n$ (units $m^{+1/3}$) is the path-integrated structure parameter. Figure 3.8 from [19] shows a representation of the DIM imaging process. Belen'kii [34, 35] established that $\hat{C}^2_n$ can be expressed

$$\hat{C}^2_n = \int_0^H C^2_n(h)(1 - h/H)^{5/3}dh, \tag{3.7}$$

where H is the distance from the laser guidestar to the source. This expression is valid for the spherical wave situation due to the finite distance from the source to the receiver. To determine $f(d/D)$, Sarazin and Roddier [20] proposed separately determining the variance along the longitudinal and transverse axes (as in Figure 3.8) of the image frame

$$\sigma^2_l = 2\lambda^2 r_0^{-5/3}[0.179D^{-1/3} - 0.0968d^{-1/3}] \tag{3.8}$$

and

$$\sigma^2_t = 2\lambda^2 r_0^{-5/3}[0.179D^{-1/3} - 0.145d^{-1/3}], \tag{3.9}$$

where λ is the wavelength and r_0 is the coherence diameter. These are the forms of Equation 2.11 solved in the transverse and longitudinal directions. Using Equation 2.10 and substituting for the coherence diameter we can arrange these expressions in the forms

$$\sigma^2_l = f_l(d/D)D^{-1/3}\hat{C}^2_n \tag{3.10}$$

and

$$\sigma^2_t = f_t(d/D)D^{-1/3}\hat{C}^2_n, \tag{3.11}$$

where $f_l(d/D)$ is the function for the longitudinal component and $f_t(d/D)$ is the function for the transverse component. These are related to the total DIM variance by

$$\sigma^2_{DIM} = \sigma^2_t + \sigma^2_l \tag{3.12}$$

which leads to

$$f(d/D) = 33.2[0.358 - 0.242(d/D)^{-1/3}]. \tag{3.13}$$

Merging Equations 3.6, 3.7, 3.13 yields

$$\sigma^2_{DIM} = 33.2D^{-1/3}[0.358 - 0.242(d/D)^{-1/3}] \int_0^H C_n^2(h)(1 - h/H)^{5/3} dh \tag{3.14}$$

which is the foundational analytic expression for the OTP system. Equation 3.14 produces a DIM variance given subaperture parameters d and D imaging a laser guidestar at a distance H away and a turbulence profile $C_n^2(h)$ along that path [19]. Equation 3.14 is called the forward model, and needs to be inverted since OTP's input is DIM variance and its output is C_n^2. To discretize the forward model, turbulence must be assumed approximately constant in each range interval of ranges h_i for $i = 1, 2, ..., n$

$$C_n^2(h) = C_j \text{ for } h_{j-1} < h < h_j \tag{3.15}$$

where $h_0 = 0$. With this approximation, Equation 3.14 can be expressed as the measurement function at distance h_i

$$M_i = \sum_{j=1}^{i} C_j \int_{h_{j-1}}^{h_j} (1 - h'/h_i)^{5/3} dh'. \tag{3.16}$$

For $j \leq i$ the integral in Equation 3.16 evaluates to

$$G_{ij} = \frac{3}{8} h_i [1 - (1 - h'/h_i)^{8/3}]_{h'=h_{j-1}}^{h'=h_j} \tag{3.17}$$

with $G_{ij} = 0$ for $j > i$. With this result the discrete forward model is written

$$M_i = \sum_{j=1}^{i} G_{ij} C_j. \tag{3.18}$$

Equation 3.18 needs to be inverted to solve for C_j. This is a challenging inversion problem since the inversion procedure must produce turbulence profiles that span several orders of magnitude from just a few measured DIM variance values. Standard matrix methods result in ill-conditioned matrices and unphysical solutions owing to the weighting function of the DIM lidar technique, shown as the solid line in Figure 3.9. However, if the measurement function can be specified analytically or with a table of smoothed values, then its derivative

$$S_i = \sum_{j=1}^{i} C_j \int_{h_{j-1}}^{h_j} \left[\frac{5}{3} h' \left(1 - h'/h_i\right)^{2/3} / h_i^2 \right] dh' \tag{3.19}$$

can be evaluated. The integral in Equation 3.19 with $j \leq i$ is

$$U_{ij} = \left[\frac{3}{8} - \left(\frac{3}{8} + \frac{5}{8} h'/h_i \right) \left(1 - h'/h_i\right)^{5/3} \right]_{h'=h_{j-1}}^{h'=h_j} \tag{3.20}$$

with $U_{ij} = 0$ for $j > i$. Now the derivative can be expressed as

$$S_i = \sum_{j=1}^{n} U_{ij} C_j \tag{3.21}$$

and the inversion is

$$C_i = \frac{i}{U_{ii}} \left(S_i - \sum_{j=1}^{i-1} U_{ij} C_j \right), \tag{3.22}$$

where each C_i is calculated in ascending order. This inversion produces stable results for a variety of DIM measurements owing to its weighting function, shown as the dashed line in Figure 3.9, which steeply approaches zero as h' approaches h and U_{ii} is much larger than G_{ii} [19]. The basis functions used to represent the measurement function $M(h)$ introduced in Equation 3.18 must be configured carefully in order for Equation 3.22 to

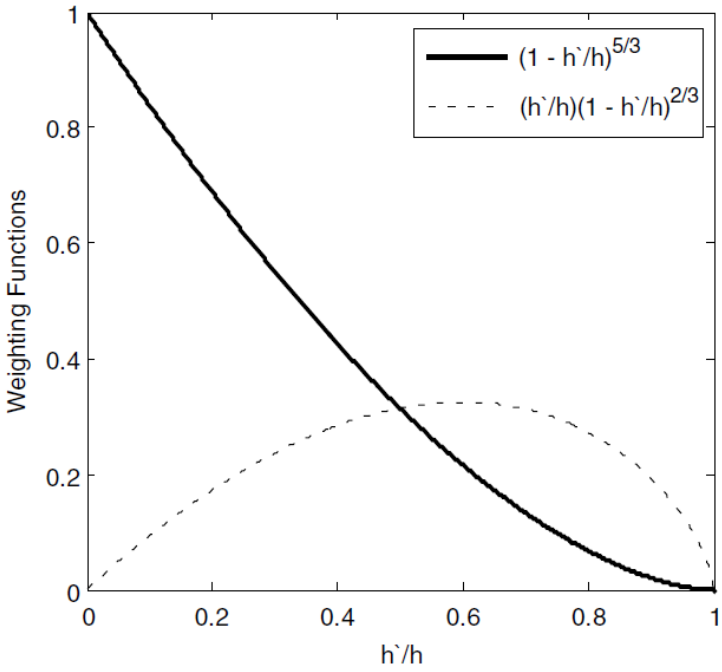

Figure 3.9: Weighting functions affecting IACS [19].

produce physical results. After some experimentation Gimmestad [19] adopted

$$M(h) = \mu_1 h/(h + b_1) + \mu_2[h/(h + b_2)]^2 \tag{3.23}$$

as the most versatile and robust (though not most accurate) form of the measurement function. The parameters μ_1, b_1, μ_2, and b_2 are determined by a least-squares fit to seven given C_n^2 data points at 0.25, 0.5, 1, 2, 4, 8, and 15 km altitude. This choice of measurement function provides a factor of 2 accuracy for measurements up to 6 km. Beyond 6 km, accuracy quickly drops off.

IACS measures the DIM variance of three laser guidestar pairs. An example image showing the averages of laser guidestar pairs is shown in Figure 3.10. The shared variance of each pair of guidestars is measured and then inverted into C_n^2. A measurement run of DIM variance at each range bin is shown in Figure 3.11. A DIM variance measurement and its associated error is expected to increase as distance increases. Figure 3.11 shows the results of a horizontal run on June 23rd across an all-grass path. Despite the gap between

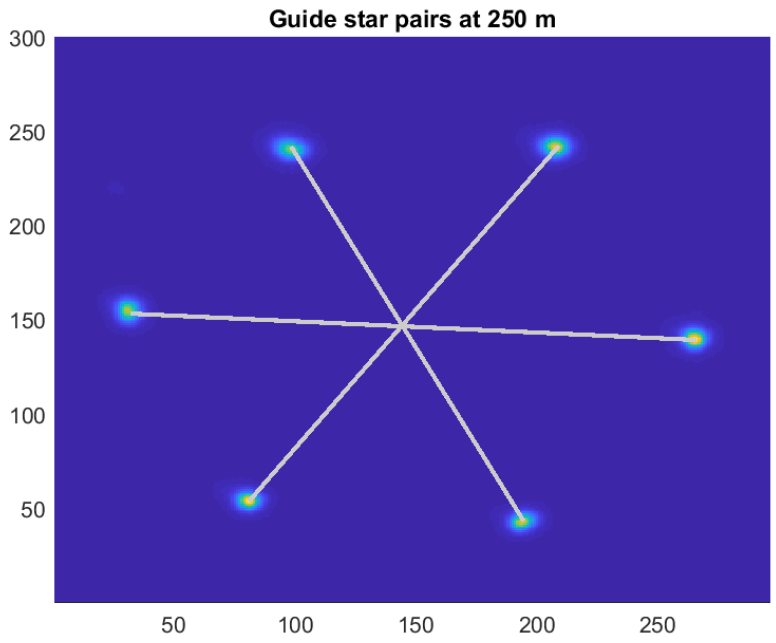

Figure 3.10: Laser guide star centroid pairs for a measurement collected at 250 m.

the two measurements at 500m, DIM variance increases with distance as expected.

3.4 System Comparison

The preceding information is summarized in Figure 3.12. Systems will be compared using this content in Chapter 6.

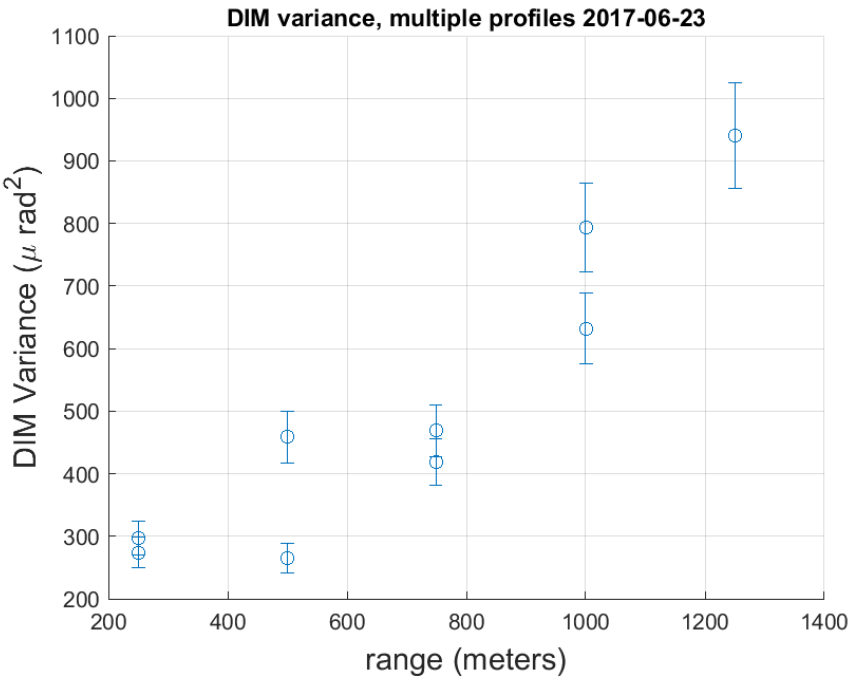

Figure 3.11: DIM Variance per range bin across grass path.

Equipment and Basis	Measured phenomenon	Measurement technique	Advantages	Disadvantages
Scintillometer (K&Z and BLS-900) Basis: Irradiance Path-Profile: No	Scintillations - intensity fluctuations of a beam of light	Variance of fluctuations used to directly calculate Cn2	Direct measurement, long-established and verified, cheap and dependable	Probabalistic nature of scintillations, saturation at high turbulence, saturation at long distances (4.5km K&Z), double-ended
PROPS, Difference of Differential-Tilt Variance (DDTV) Basis: Phase Path Profile: Yes	Measures DTVs or tilt covariances from wavefronts of a source across a path, which are converted to weighted integrals of Cn2	Known weighted integrals of Cn2 and compared against the DTV measurements, then DTV's are inverted to produce Cn2 estimate	Can detect changes in turbulence along path resulting from the surface features along path, estimates cross-wind speeds as seen from both sides of path.	Double-ended, requires constant monitoring since two units must communicate results
DELTA, modified DDTV Basis: Phase Path Profile: Yes	Computer measures the differential jitter of feature pairs as a function of angular separation	Image processing techniques used to estimate Cn2 from jitter	Semi-single ended with appropriate high-contrast scene, immune to many sources of error, easy to deploy	Less accurate than PROPS
IACS, Differential Image Motion (DIM) lidar Basis: Phase Path-Profile: Yes	Centroid of artificial star determined in each aperture, and image variances of each centroid are captured for each aperture	Total variance of these separate centroid variances is measured and used to directly calculate r0	Truly single-ended, eliminates sources of error by using multiple apertures and source beams, slant-path measurements possible	Large, difficult to deploy and operate, expensive, LCH required for vertical measurements

Figure 3.12: Summary Comparison of devices presented.

CHAPTER 4

THE DATA COLLECTION AND INSTALLATION OF THE SYSTEMS

A recent experiment to collect C_n^2 had two purposes: (1) to establish a level of confidence and performance envelopes of equipment relevant to measurement of atmospheric characteristics to be used to support operations; (2) to gauge potential performance of this equipment in characterizing the atmosphere at the littoral zone. The littoral zone (land-sea boundary) has a strongly inhomogeneous atmospheric structure due to its constantly changing temperature, pressure, wind conditions, and surface conditions. The experiment was conducted at the NASA Shuttle Landing Facility (SLF) in Cape Canaveral, FL from June 20-28, 2017 and is referred to as The Comprehensive Atmospheric Boundary Layer Extinction / Turbulence Refinement Analysis EXperiment (CABLE-TRAX). CABLE-TRAX was designed around IACS since it is still a prototype and not a production system. CABLE-TRAX presented an opportunity to test other atmospheric measurement systems alongside IACS, including production-ready systems such as PROPS and DELTA. This section describes the test and setup of all systems for reproducibility purposes and to highlight opportunities for an improved test [36].

4.1 NASA SLF and General Geography

The NASA SLF is a restricted access facility in the Kennedy Space Center with its own controllable air space. The restricted airspace combined with a 5km precision-leveled runway, shown in Figure 4.1, make this an ideal location for C_n^2 measurements. The controllable air space was needed to facilitate IACS' vertical lasing windows as determined by the Laser Clearing House (LCH). The level path of relatively constant elevation gives greater confidence to turbulence measurements taken across it since turbulence strength varies with elevation. All path-dependent measurements were conducted first over the grass to the left

Figure 4.1: NASA SLF runway [37].

of the runway (shown in Figure 4.1), so that the lasers and all other measurement equipment measured turbulence solely above grass. Measurements over generally flat ground that is all the same surface should match C_n^2 trends. The measurements were then performed again above a path that was partially grass and partially runway. There should be a change in C_n^2 along this multi-surface path, especially when compared to the previous measurements across the exclusively-grass path. Data collected along this multi-surface path was used to test IACS' "slabbing" capability. This capability allows IACS to assign different C_n^2 values to different slabs of the path based on the surface of the slab.

The equipment under test for measuring C_n^2 was co-located, as shown in Figure 4.2. A backstop was erected 1.5 km from this firing site. The backstop consisted of two conex boxes covered in black landscaping fabric sitting behind a beam dump, a plywood structure angled such that a laser beam would be directed down to the ground. The backstop, beam dump, and some of the receiver ends of certain equipment is shown in Figure 4.3.

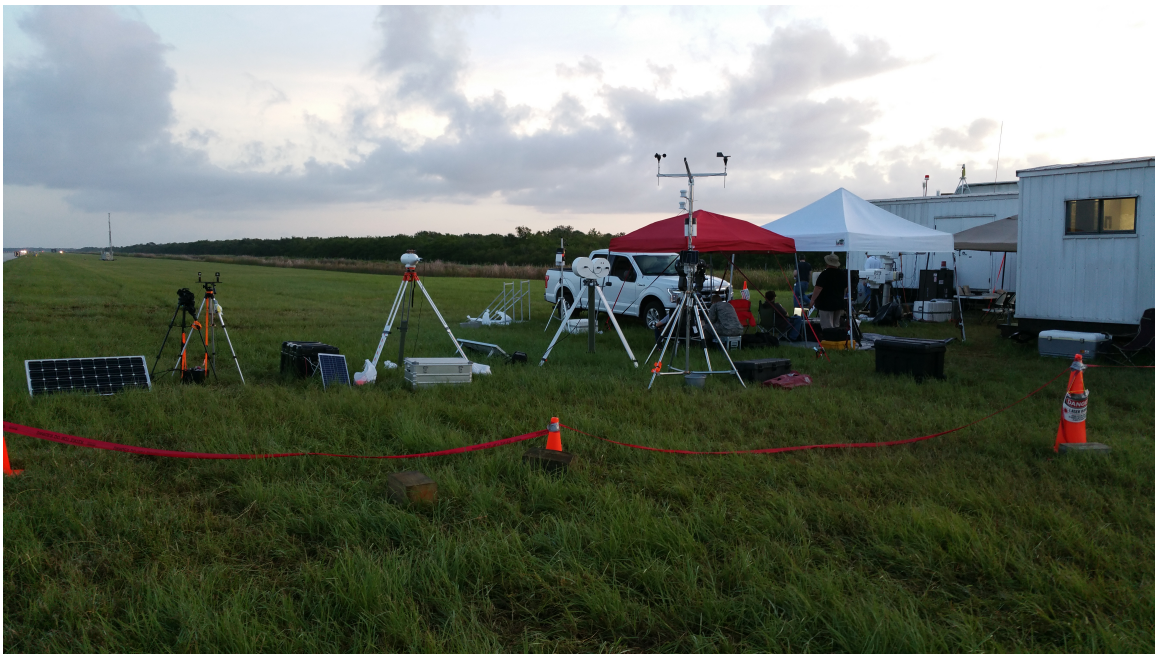

Figure 4.2: Various sensors pointing downrange.

Figure 4.3: The backstop (beam dump).

4.2 Scintillometer

The Kipp & Zonen (K&Z) Large Aperture Scintillometer (LAS) unit, seen in Figure 3.1 was set up in front of the IACS laser shelter and connected to the IACS shelter's power and data inputs. The LAS output voltages were read into and stored via the IACS auxiliary data panel. Setup involved mounting the unit on a tripod approximately 2.5 m high and pointing it in the direction of the backstop. The second unit was placed next to the backstop on its own tripod, powered by a portable battery. The two separate scintillometers must be aligned, a process of rotating and adjusting the second unit in increasing levels of precision until the power received by the first unit reaches an acceptable minimum level. Once set up, the system is designed to run continuously without further maintenance. The portable battery powering the second unit was changed occasionally. When the backstop was moved across the runway, the second unit was moved alongside it, and the calibration procedure was repeated. Setup of the BLS-900 followed a similar procedure.

4.3 DELTA

The DELTA system consists of an imaging unit and a high-contrast target board. The imaging unit, shown in Figure 3.5 consists of a telescope, tripod, camera, and computer. There were two DELTA systems at the test, arranged opposite one another as shown in Figure 4.5 . The first imaging unit was placed near IACS with its target board near the backstop. The second imaging unit was placed right next to the target board of the first unit, and its target board sat next to the first unit. The target boards, seen in Figure 4.4 were placed in truckbeds to keep them elevated off the ground. This was to avoid the strong anisotropic turbulence close to the ground. The camera images the target board and measures the differential jitter of feature pairs as a function of angular separation. Software on the computer shows some real-time data and diagnostic results, but little maintenance needs to be performed after initial setup.

Figure 4.4: The DELTA high contrast target board.

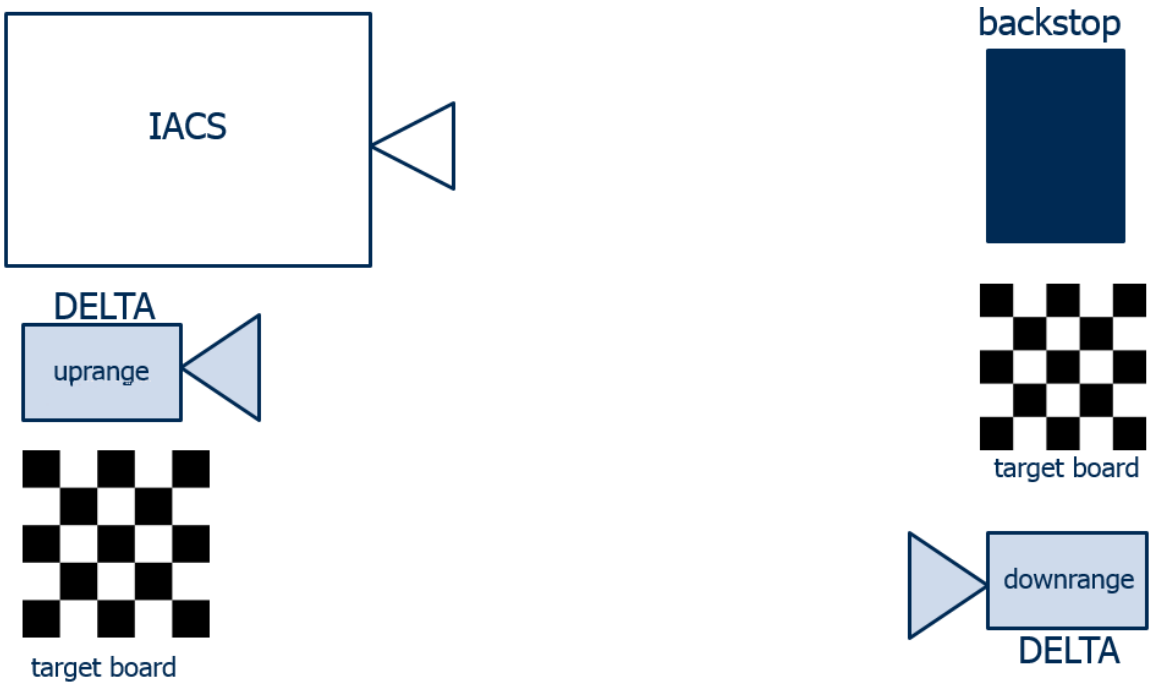

Figure 4.5: Demonstration of how the two different DELTA systems were set up relative to IACS.

4.4 PROPS

The PROPS system consists of two units aimed at each other. Each unit, shown in Figure 3.4 consists of a telescope, tripod, LED assembly, wavefront sensor assembly, and computer. The units were separated by 1.5km, with one unit near IACS and the other unit near the backstop, unlike the DELTA systems. The units face each other, and image each others' LED assemblies across the path, with the turbulence-induced deviations recorded on computers. The alignment process is more involved than the DELTA system. Each telescope must precisely focus the LED sources onto the wavefront sensor assembly. Software on the computer assists the operator with this task. Real-time measurements are broadcast across the path to a designated "master" computer. This master computer incorporates the data being sent in this manner into the model that evaluates turbulence measurements across the path. Proper alignment and the wireless data connection must be maintained throughout the entirety of the test. This proved difficult during the CABLE-TRAX collection because downrange operations were ceased when ever the IACS lidar lased horizontally.

4.5 IACS OTP

IACS consists of two shipping containers: one housing personnel and controls and the other housing the optics systems. IACS has multiple lidar subsystems that include a water vapor profiler, aerosol profiler, and optical turbulence profiler. In order to lase vertically, the air space must be free of planes and other aircraft, and specific vertical-firing times were sent to the IACS team from the laser clearing house and coordinated with the air traffic control tower at the NASA SLF. These firing windows varied by day. When the team was not allowed to lase vertically, the system was rotated to lase horizontally 1.5km into the backstop shown in Figure 4.3. The IACS system used three different laser beams, each of which had to be walked out to the backstop. The walk out process is as follows: each beam was fired into a rental truck which had the inner rear wall painted with non-

reflective paint. The truck progressed slowly toward the backstop as each laser system was aligned and tested along the way. Once the beam reached the backstop, the coordinates for the dead center and the vertical and horizontal limits of the backstop were hardcoded for the remainder of the test. This setup process was repeated when the backstop was moved across the range to collect variable-path data. One unfortunate issue that could not be resolved was noon-time vertical windows. With the sun directly over IACS, no noon-time vertical windows could be utilized because the sun washed out the laser guidestar and presented a risk of being focused by the optics in the reverse direction and onto the equipment. When the team was outside of vertical windows, the laser assembly was rotated and fired horizontally into the backstop, within the hard limits determined during setup. Due to the wavelengths of IACS' lidar subsystems, laser eye protection had to be worn by all personnel on the range any time IACS fired (vertically or horizontally).

The actual lasing process was conducted in the control shelter. A set of ranges was specified, and then a run was initiated. A run consists of the laser guidestars being focused at each distance specified (typically 250m to 1250m in steps of 250m) and the DIM variance measured. Taking measurements at these specific ranges produces a range-resolved turbulence profile. The system cycles through the ranges specified in a run, and runs can be manually initiated or automated.

CHAPTER 5

RESULTS

The results of the data collection are divided between general comparable attributes and more system-specific measurements. Path-averaged C_n^2, defined in Chapter 2, is used to compare the C_n^2 measurement systems. The comparison is best shown by overlaying the results of the data collected each day.

5.1 Path-averaged C_n^2

The path-averaged C_n^2 results are displayed per day. Figure 5.1 shows data taken by PROPS, DELTA, IACS, the K&Z LAS, BLS-900, and METAR data reported by the NASA SLF Air Traffic Control tower each day of the test. The NASA SLF was closed on Sunday June 25, 2017.

5.1.1 The Daily Trend of Turbulence Strength

C_n^2 measurements generally follow a daily trend. An example of the standard turbulence trend is shown in Figure 5.2 from [30], where turbulence rapidly increases from the "stable" overnight trend to the "unstable" daytime trend. C_n^2 measurements must be taken throughout the day to determine conformance to this trend, and deviations from this trend happen regularly but must have a valid explanation, such was wind velocity changing in direction

Equipment/Date	6/20/2017	6/21/2017	6/22/2017	6/23/2017	6/24/2017	6/25/2017	6/26/2017	6/27/2017	6/28/2017
K&Z LAS	No	No	No	No	No	No	Yes	Yes	No
IACS OTP	No	No	No	Yes	Yes	No	Yes	Yes	Yes
DELTA	Yes	Yes	Yes	Yes	Yes	No	Yes	No	No
PROPS	Yes	Yes	Yes	Yes	No	No	No	No	No
BLS-900	Yes	Yes	Yes	Yes	Yes	Yes	Yes	Yes	No
METAR	Yes	Yes	Yes	Yes	Yes	Yes	Yes	Yes	No

Figure 5.1: Data Collected by system and day.

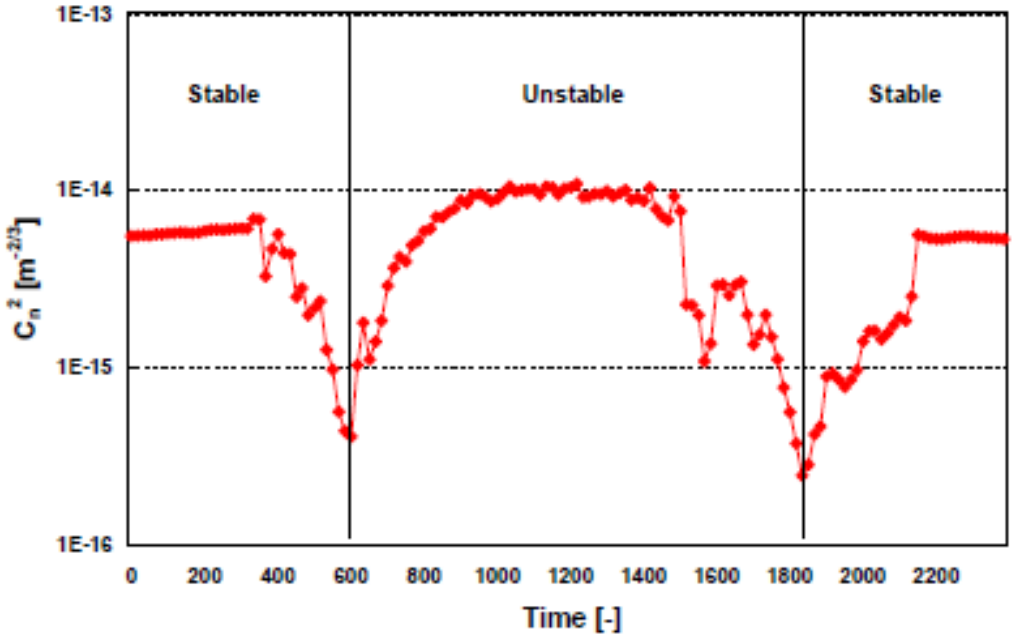

Figure 5.2: Typical diurnal trend for C_n^2 measurements [30].

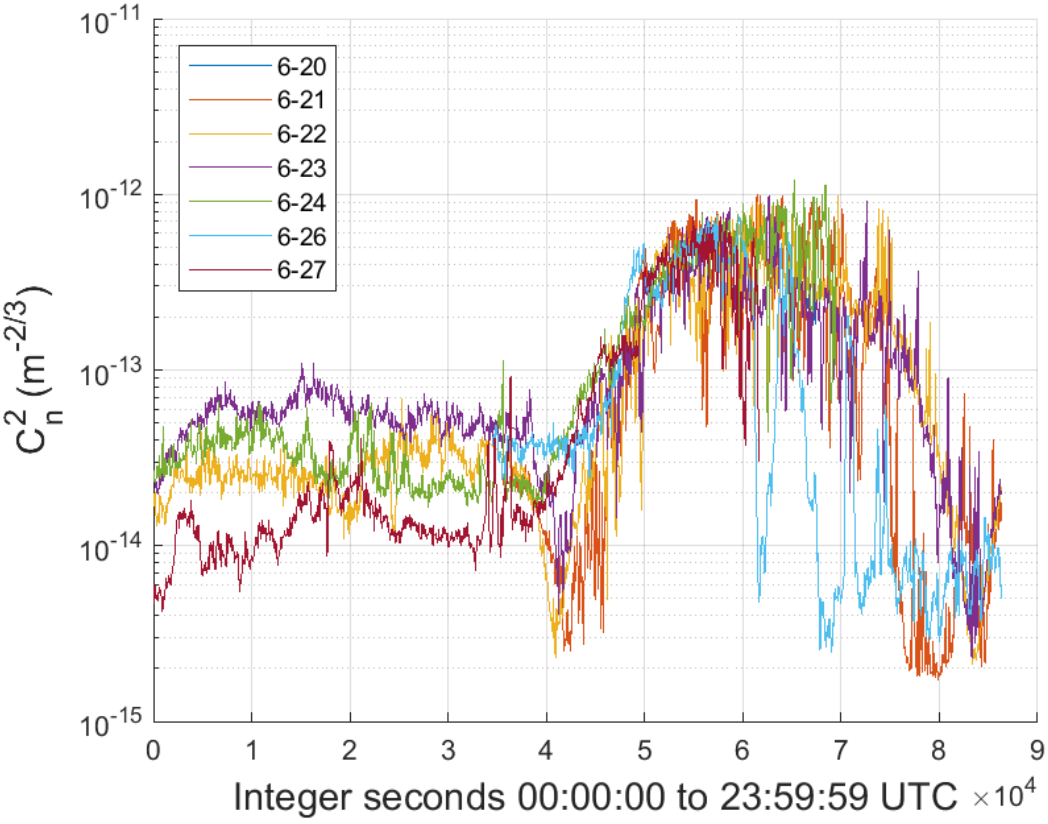

Figure 5.3: Every day of BLS-900 measurements overlapped.

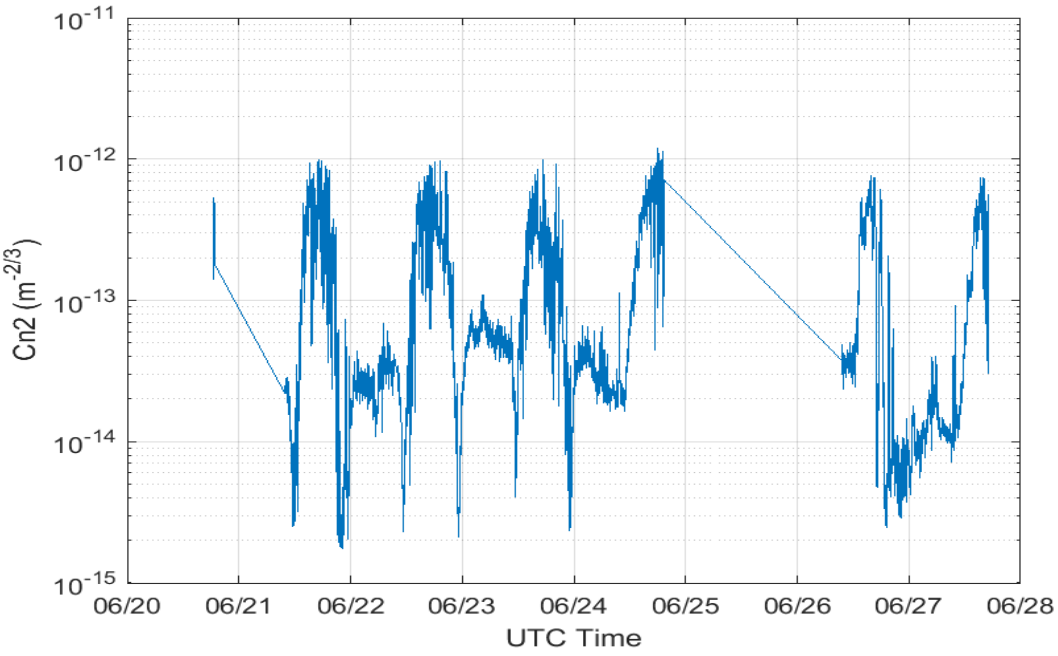

Figure 5.4: Every BLS-900 measurement taken during the test.

or magnitude, a temperature gradient forming or dissipating, or a change in humidity reflected by the temperature shifting relative to the dew point temperature. Many of these trends can be observed in METAR data. The BLS-900 scintillometer ran constantly for almost all of the test. Figure 5.4 shows every BLS-900 C_n^2 measurement taken during the CABLE-TRAX test. The large gap on June 25 is due to the SLF being closed. Figure 5.4 should demonstrate a condensed week-long repetition of Figure 5.2. In order to evaluate that claim, Figure 5.3 was created. The x-axis is an integer representation of midnight to midnight UTC (20:00 to 20:00 local) of each day. The y-axis is still path-averaged C_n^2. The unstable regime on the right lives up to its name. Even the stable overnight regime has up to a factor of 10x difference between the lowest- and highest-strength days. During stable conditions, the mean is lower and standard deviation is lower than during unstable conditions. Physically explained, with no sun and no clouds to sometimes cover up the sun, the environment gradually cools overnight (rather than changing rapidly in either direction throughout the day), and C_n^2 therefore remains stable. One thing to keep in mind is that

these results are likely totally accurate. Due to optical turbulence's stochastic nature and the fact that it can be influenced by so many different atmospheric conditions, the day-to-day changes seen here are perfectly reasonable. As discussed in Chapter 3, scintillometers directly measure the variance of scintillations of a reference beam. This leads to saturation and sensitivities that phase-based C_n^2 measurement devices are immune to. The results presented in this chapter will show if this claim that phase-based results are more accurate is borne out in the field.

5.1.2 June 20, 2017

June 20 was considered a setup day for most of the systems and equipment. However, DELTA and PROPS collected data as shown in Figure 5.5. The limited amount of measurement time does not provide insight into C_n^2 trends. For Figure 5.5, "DELTA up" refers to the DELTA system pointed uprange, while "DELTA down" refers to the system oriented in the opposite direction. Each data point is the average of specific measurements along the path (i.e. the path-averaged turbulence measurement). Because there are so many measurements, a 10-point rolling average is presented to smooth the results of the DELTA and PROPS systems. The rolling average is taken by averaging the first ten measurements, then taking a new average for each new data point by popping off the oldest data point and re-averaging with the newest data point. This unfortunately smooths out the data but makes for less repulsive figures. The small amount of data in 5.5 captures the drop in C_n^2 at the late afternoon as turbulence moves from the unstable daytime regime to the stable nighttime regime, matching the right-hand side of Figure 5.2. Most test days concluded before sunset or even this change could be observed.

5.1.3 June 21, 2017

Figure 5.6 shows DELTA and PROPS results of path-averaged C_n^2 as a function of time. There are no IACS results because the team was still setting up the system. The rolling av-

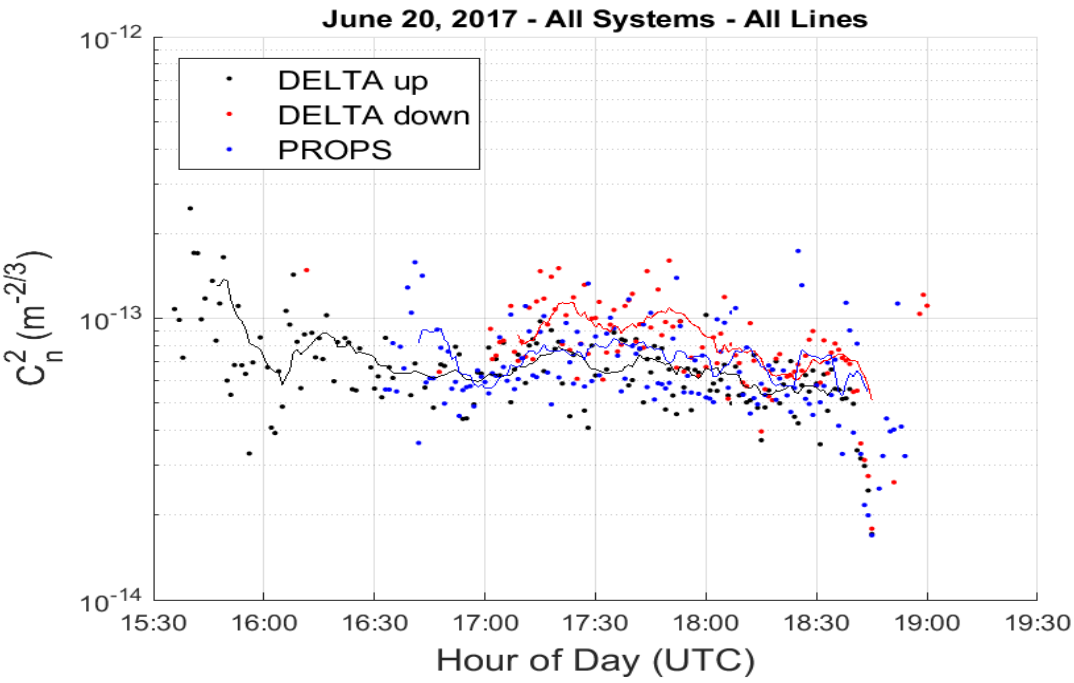

Figure 5.5: Path-averaged C_n^2 on June 20 across all operational systems. Solid lines are 10-point rolling averages.

erage calculated results are included as well. There are some gaps in PROPS data this day that can be attributed to system failures near the backstop that could not be addressed because the IACS team was horizontally lasing. In the interest of laser safety, personnel could not be downrange while IACS OTP lased horizontally. The observed measurements still show us that phase-based systems generally agree with each other in magnitude for most of the day. The standard turbulence trend can be observed in Figure 5.6. The systems demonstrate the daily rise, noting that UTC is four hours ahead of local time for the data collection (EDT). Measurement stopped as soon as C_n^2 was about to drop into the stable nighttime region. The measurements never differ by more than an order of magnitude and visually agree in trend. The smoothing effect of the rolling average operation eliminates some of the sharp drops in turbulence strength. The included BLS-900 scintillometer results reveal that these drops are not noise but are measured by the systems. There is maximally an order of magnitude disparity between the phase-based systems and the scintillometer during the unstable daytime measurement time.

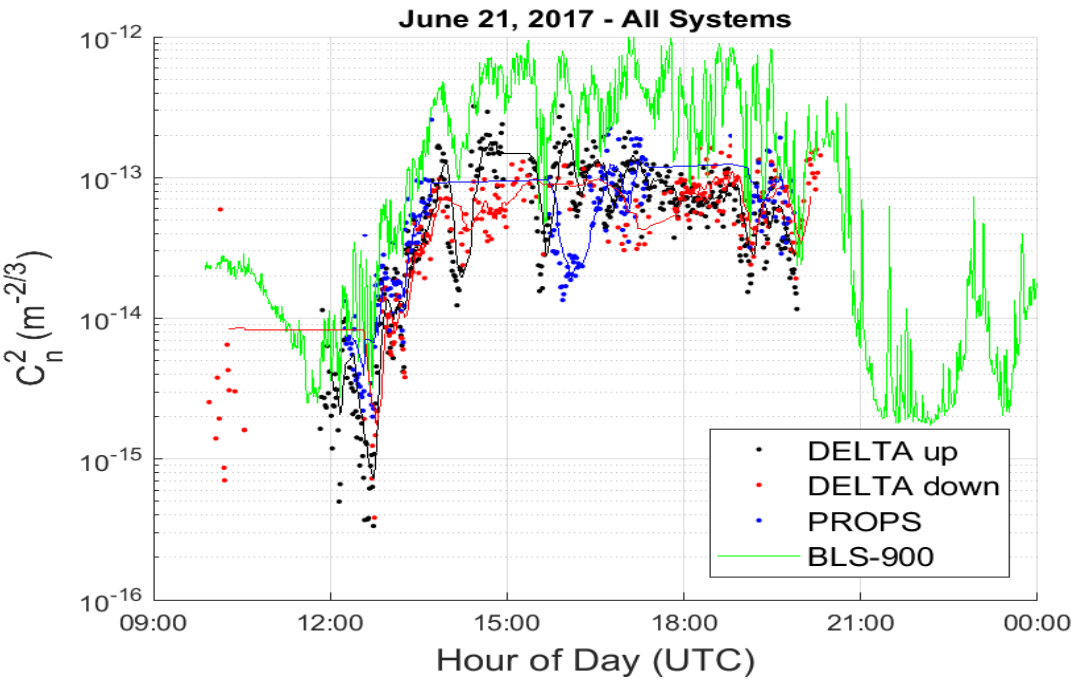

Figure 5.6: Path-averaged C_n^2 on June 21 across all operational systems. Solid lines are 10-point rolling averages.

5.1.4 June 22, 2017

Figure 5.7 shows the results from DELTA and PROPS operations and BLS-900 scintillometer measurements. The same general trend is still observed that C_n^2 changes from low values in the cooler late evening/early morning to steady higher values throughout the day. There is a tremendous drop in turbulence in the early morning, where DELTA records an order of magnitude less turbulence strength than the scintillometer. To determine if that early morning drop is a fluke of the DELTA uprange system or an actual measurement of importance, I reviewed the METAR data shown in Figure 5.8 for that observation time. There is a drastic change in wind direction and a gradual drop in wind speed at the measurement time, combined with gradual meeting of the temperature and dew point temperature. This stillness could account for an unusually low turbulence measurement. As the temperature and dew point temperature separate and the wind speed picks back, C_n^2 rises as expected. Beyond the early morning measurement, there is a typical magnitude disparity between the

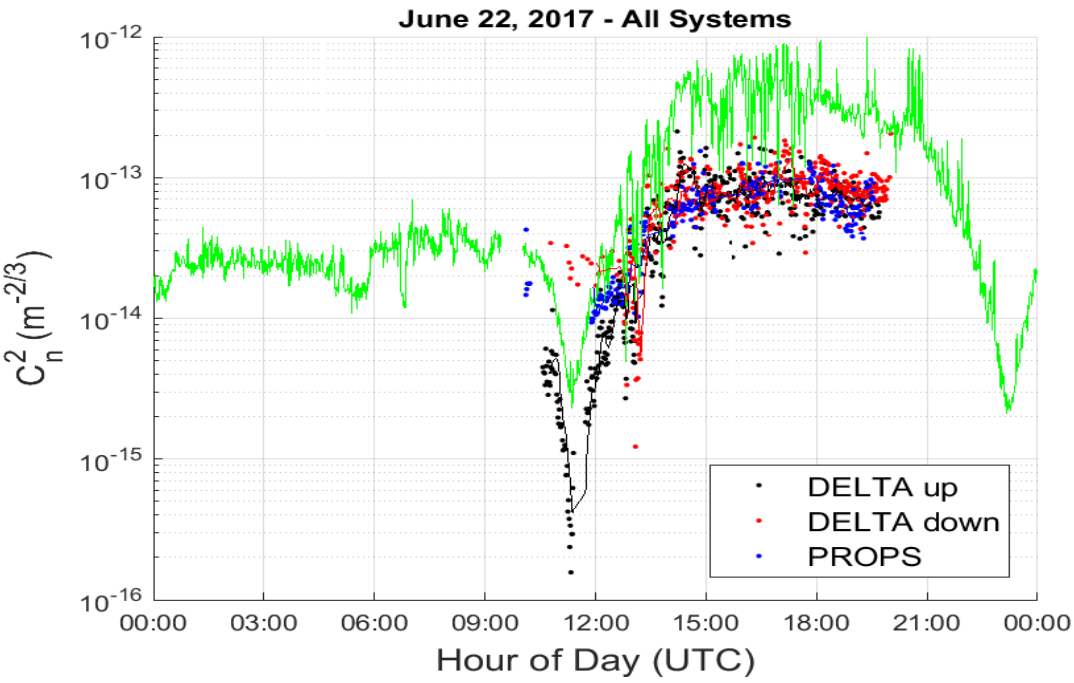

Figure 5.7: Path-averaged C_n^2 on June 22 across all operational systems.

phase-based systems and the scintillometer of 2x during the rising period and 5x at the end of the day.

5.1.5 June 23, 2017

On June 23, IACS OTP, DELTA, PROPS, and BLS-900 measurements are shown in Figure 5.9. IACS OTP measurements are path-averaged like DELTA and PROPS, but the path specified is from the laser to the end of the range bin, i.e. the distance to which the laser is focused and which the measurements are taken across. Thus the only relevant measurement for comparison from IACS is the 1.25 km measurement, as PROPS and DELTA measured across the 1.5km test range. DELTAs and PROPS again capture the sunrise trend while measuring less magnitude than the scintillometer. The few IACS data points also match the phase-based devices while agreeing with the scintillometer trends. Figure 5.10 zooms in on the portion of the day containing IACS measurements. The rolling average of PROPS and DELTA data has also been removed to provide a fairer comparison of trends. There is a

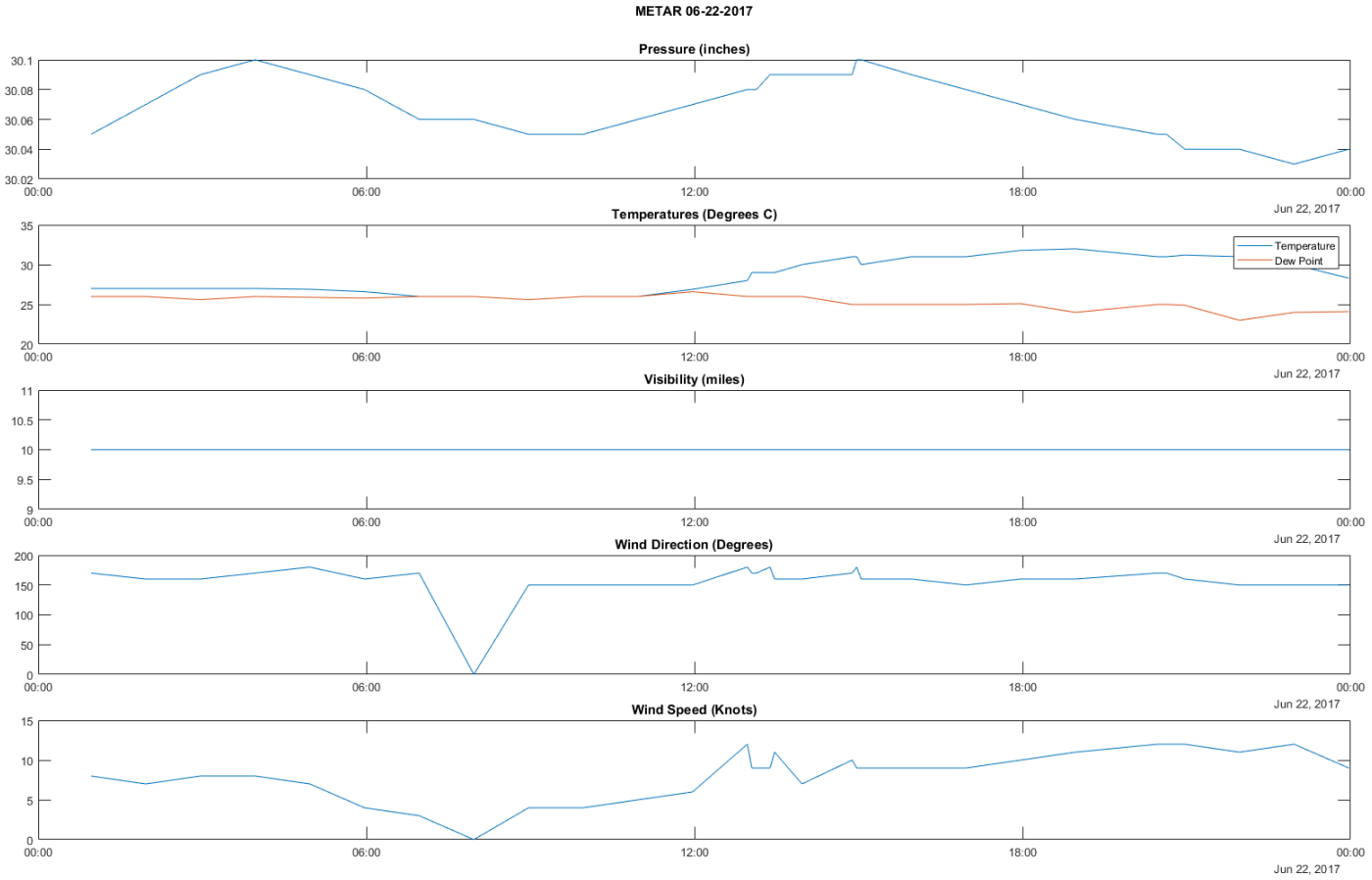

Figure 5.8: METAR data for June 22, 2017 as reported by SLF tower.

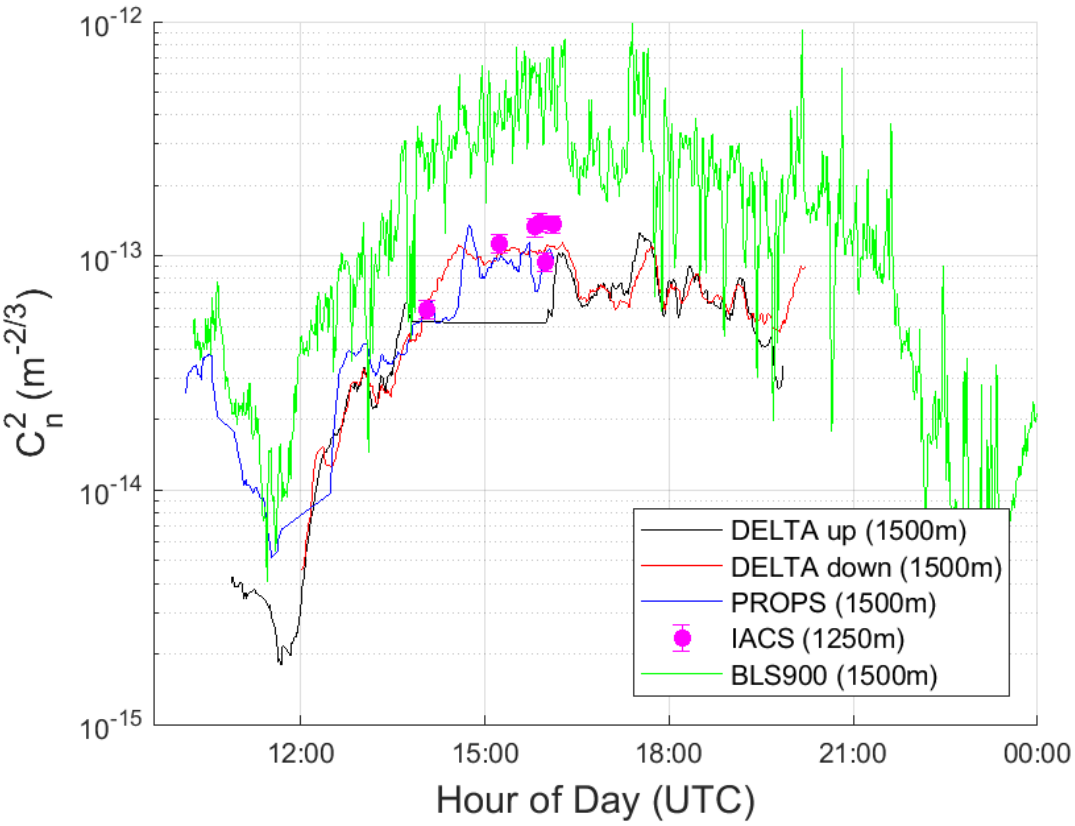

Figure 5.9: Path-averaged C_n^2 on June 23 across all operational systems.

magnitude disparity of 4-6x between the IACS measurements and the scintillometer. There is a less than 2x disagreement between IACS and the other phase based systems. IACS OTP was designed with vertical measurements in mind. Calculating horizontal turbulence from DIM variance is a matter of holding C_n^2 constant as seen in Chapter 3. For vertical measurements, outer scale L_0 (the maximum size of the largest turbulent eddies) can be assumed infinite and ignored. However, for horizontal measurements near the ground, L_0 is definitely finite. Ignoring could negatively affect IACS C_n^2 measurements since the L_0 insensitivity mentioned in Chapter 2 is only true for vertical measurements.

5.1.6 June 24, 2017

On June 24, the PROPS team left and the K&Z scintillometer was still not operational, so IACS OTP, DELTA, and BLS-900 results are shown in Figure 5.11. The horizontal lasings

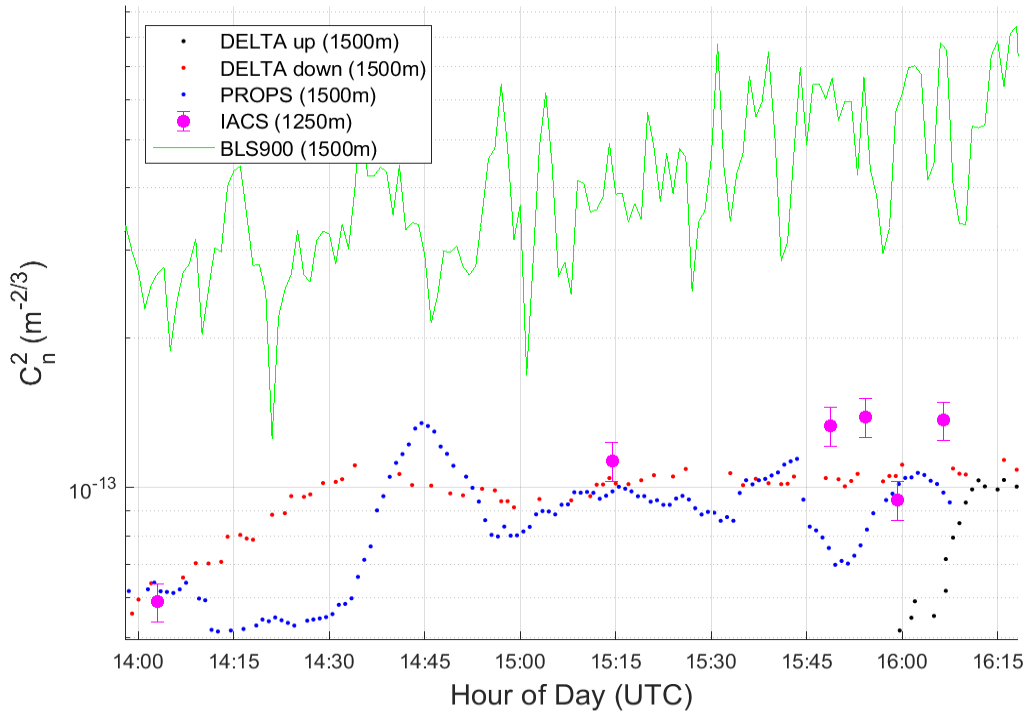

Figure 5.10: Path-averaged C_n^2 on June 23 focused on the time of IACS' lasing.

tend to agree with the DELTA systems. The daily trends repeat with the scintillometer measuring stronger magnitude than the phase-based systems. Figure 5.12 shows the zoomed-in results of the first relevant IACS data collection. Here I would like to highlight the difference in the DELTA systems' results. The reason they disagree in magnitude is due to their path-weighting function and opposite orientation. In Chapter 3, a representative path-weighting function for the DELTA system is described. It favors measurements taken near the receiver, and zeros out measurements taken near the target. Placing the DELTA instruments opposite one another gives insight to the distribution of turbulence along the path even though the measurement is the path-averaged C_n^2. We can thus say that the turbulence across the path is concentrated farther downrange since the DELTA downrange system reports a higher C_n^2. Additionally in Figure 5.12 we see that IACS follows the rises and falls of the BLS-900, albeit at a lower resolution. Figure 5.13 tells the same story. IACS matches the magnitude of the two DELTA systems and captures the same sudden drops in

turbulence strength that the scintillometer reports. There is a magnitude disparity of 2-3x between IACS and the scintillometer for the left trail of IACS measurements in Figure 5.12. This same portion of IACS measurements never differs from DELTA up by more than 2x, however, when DELTA down sharply increases, the measurement disparity increases to 3x. Similar ratios hold for the 3-point cluster between 13:30 and 14:00. The left measurements of Figure 5.13 tell the same story with 2-3x difference between IACS and the BLS-900 and IACS and DELTA matching on magnitude. As for the dramatic drop in C_n^2 at 18:00, DELTA up totally ignores it while IACS and the BLS-900 track it. IACS-scintillometer ratio varies from 2-5x during the drop, but grow to 10x at the trough. Though IACS and the BLS-900 match in trend, the magnitude difference does not stay consistent through dramatic turbulence effects. Because these drops are so sudden, the data almost becomes a comparison of the rate of change of the fundamental phenomenon. Thus the rate of change of scintillations differs from the rate of change of DIM variance, resulting in the observed growth of the magnitude difference.

5.1.7 June 26, 2017

Measurements resumed on June 26. DELTA, IACS OTP, the BLS-900, and the K&Z LAS scintillometer were fully operational. Figure 5.14 shows the overview of the day. The BLS-900 measures much stronger turbulence than either the K&Z or the phase-based systems. This is the biggest measurement gap observed at the test at about an order of magnitude difference between the BLS-900 and the DELTA systems. Figure 5.15 zooms in on this pre-sunrise gap in the results. IACS also measures stronger turbulence. This is due to the magnification settings (adjusting the field of view) of IACS' optical systems. All previous measurements and the measurement run from 1607-1620 were conducted at the "low-mag" setting with a field of view (FOV) of 11.56 μrad. The measurement run from 1040-1140 was conducted at the "medium-mag" setting with FOV 4.08 μrad. The IACS OTP system operator can choose to adjust the FOV if he thinks the laser guidestars will not get properly

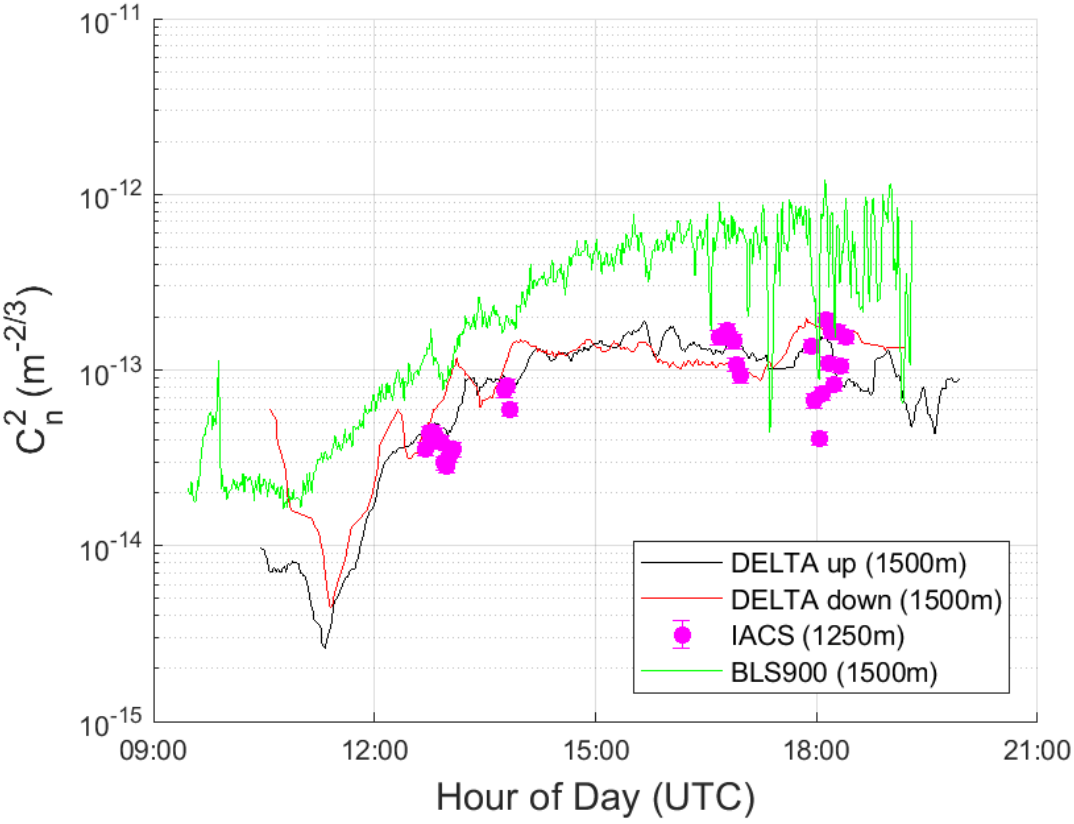

Figure 5.11: Path-averaged C_n^2 on June 24 across all operational systems.

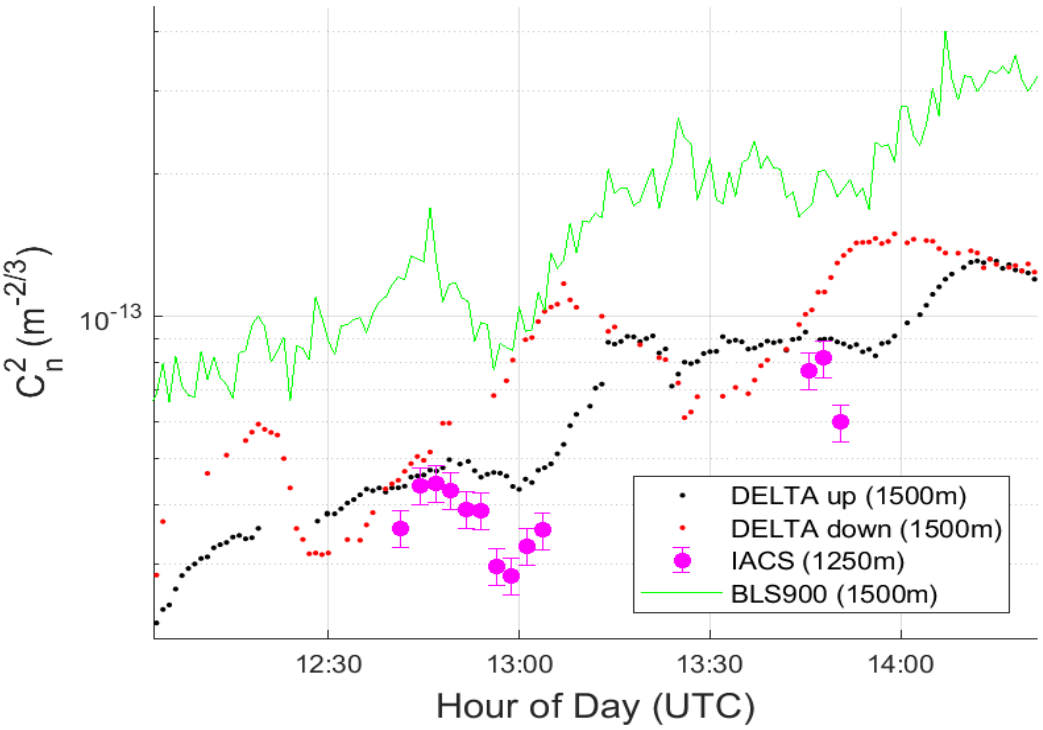

Figure 5.12: Path-averaged C_n^2 on June 24 focused on the time of IACS' first lasing.

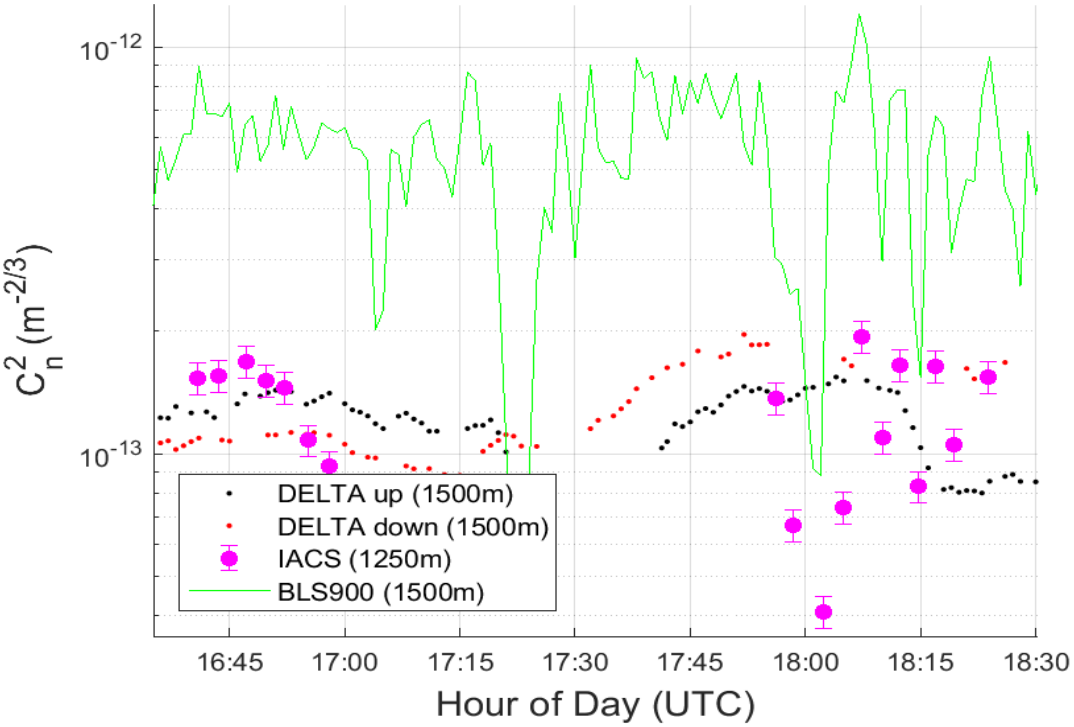

Figure 5.13: Path-averaged C_n^2 on June 24 focused on the time of IACS' second lasing.

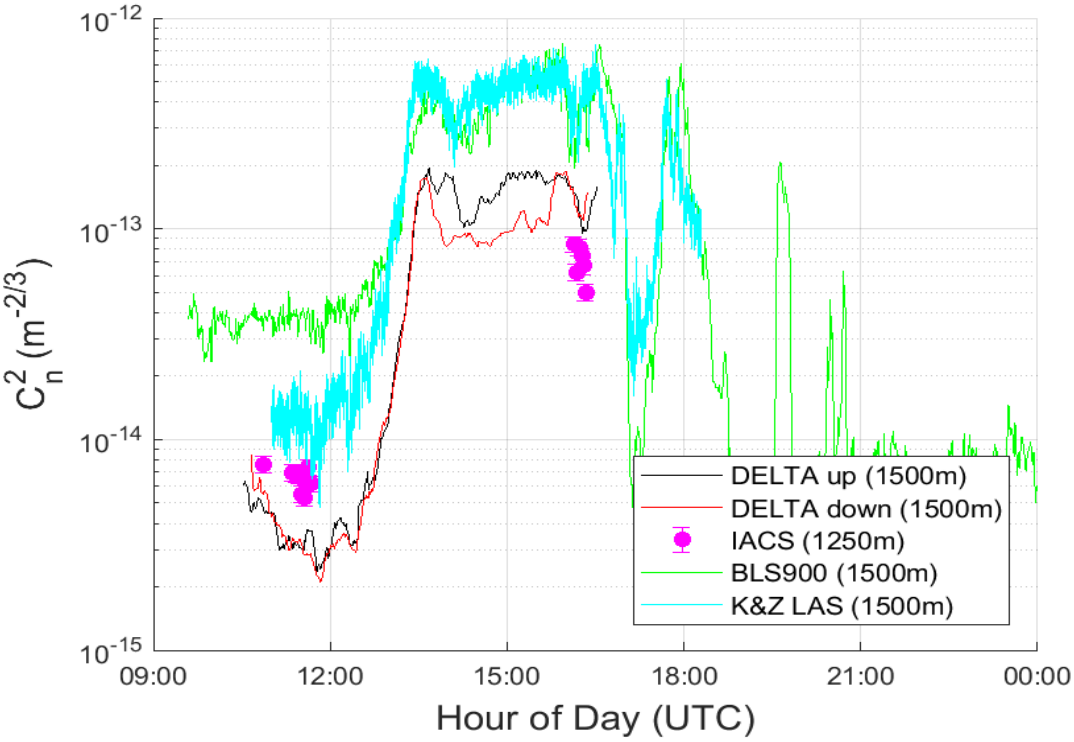

Figure 5.14: Path-averaged C_n^2 on June 26 across all operational systems.

resolved by the imaging system. The FOV was changed for this run to see how it would affect the measurements, even though the stars can be fully resolved at the low-mag setting. For this horizontal lasing at 1.25 km, decreasing FOV causes turbulence to be measured stronger than at low-mag settings. IACS measurements are 5x lower than BLS-900, 2x lower than K&Z, and 2x higher than DELTA. Since the laser guidestars were fully resolved at low-mag settings, the low-mag FOV is most appropriate for this data collection. I therefore dismiss this set of IACS measurements since they were taken with different settings than all other IACS data presented in this thesis. Figure 5.16 shows the other IACS collection from this day. The same magnitude trends observed throughout the test are back in place. The K&Z is much higher resolution than the BLS-900, and they agree in magnitude but not in small adjustments. IACS again tracks the drops of the BLS-900. Both scintillometers agree in magnitude and IACS tracks at a factor of 5x below them while remaining a factor of 2x below the DELTA measurements.

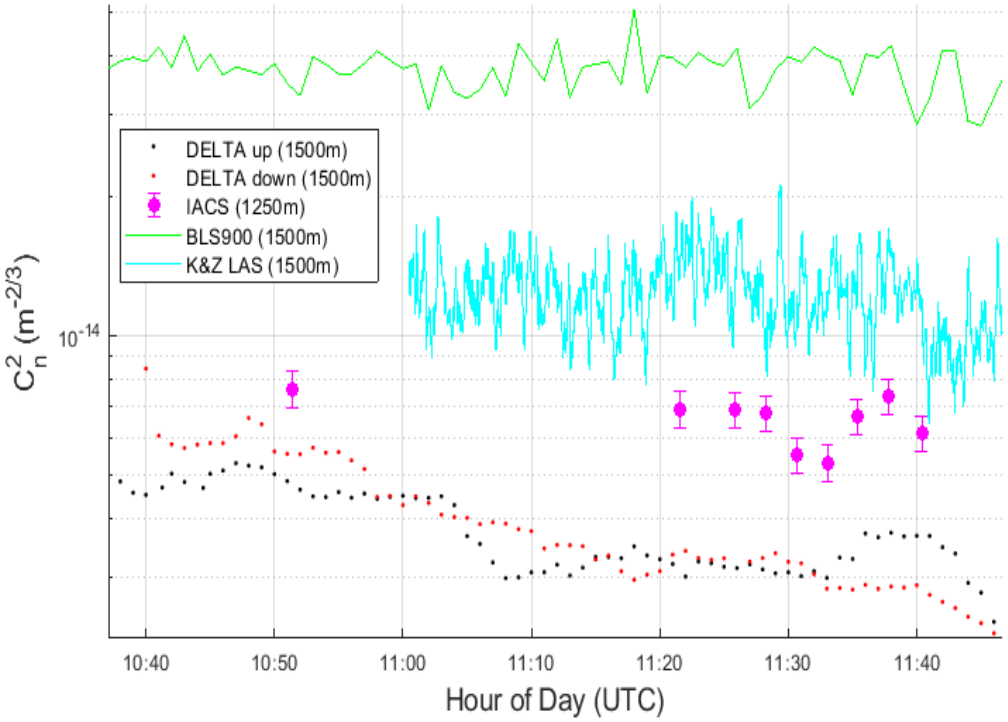

Figure 5.15: Path-averaged C_n^2 on June 26 focused on the time of IACS' first lasing.

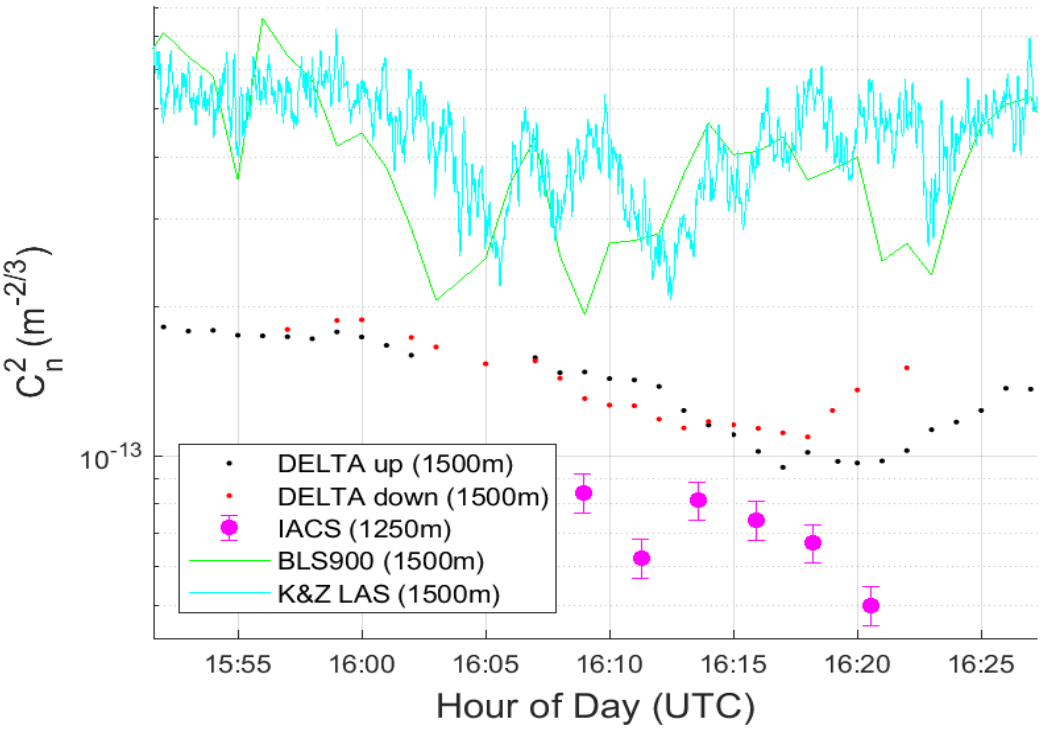

Figure 5.16: Path-averaged C_n^2 on June 26 focused on the time of IACS' second lasing.

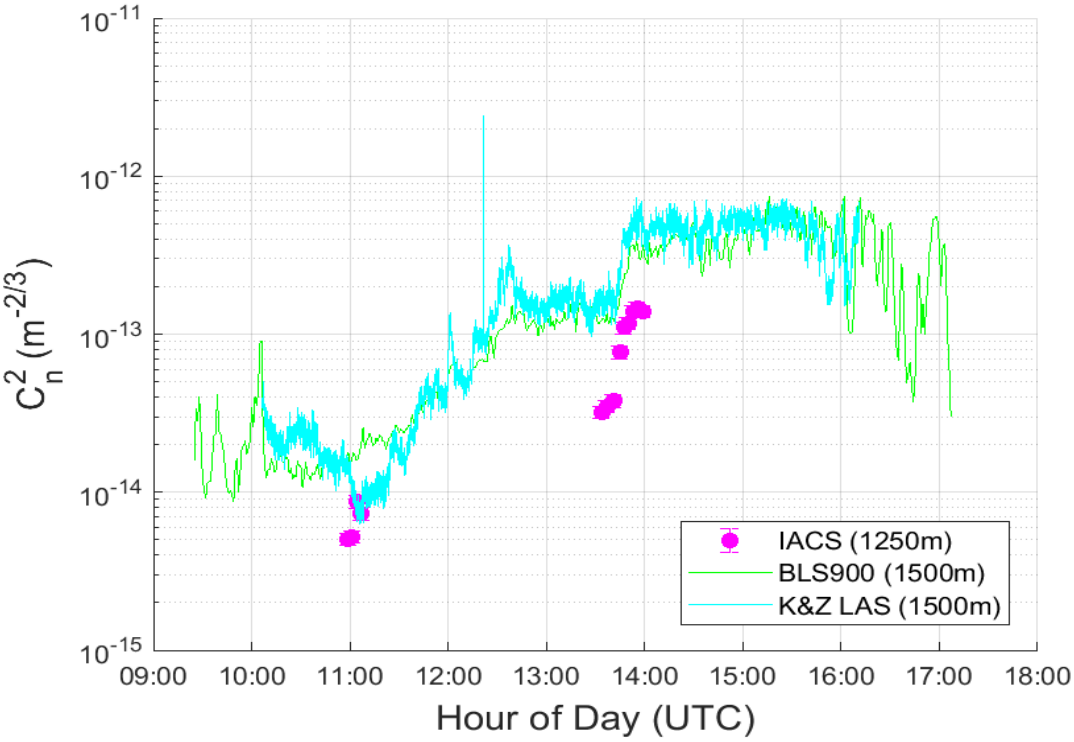

Figure 5.17: Path-averaged C_n^2 on June 27 across all operational systems.

5.1.8 June 27, 2017

On June 27, the DELTA teams departed, leaving only IACS OTP and the two scintillometers. The measurement results are shown in Figure 5.17. All IACS measurements were taken at the low-mag FOV. IACS OTP measures weaker turbulence at about the same rate as Figure 5.14. It rises along with the K&Z LAS during the 1330-1400 measurement run. Figure 5.18 captures the K&Z dropping slightly before rising into the unstable daytime zone. Prior to the drop, the two scintollometers agree and remain 2-3x over IACS. After the drop, IACS and the K&Z agree and remain 2x below the BLS-900. Figure 5.19 displays a beautiful track of IACS and the scintillometers. IACS remains within 2-3x of the BLS-900 and 3-4x of the K&Z for the entire 15 minute collection.

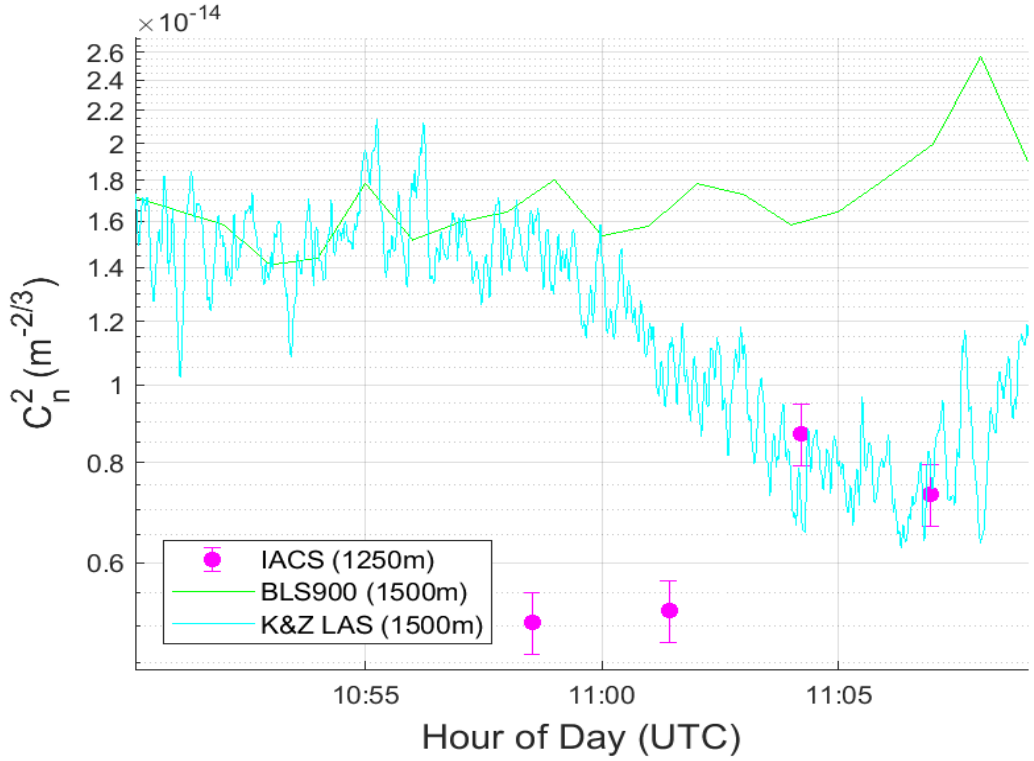

Figure 5.18: Path-averaged C_n^2 on June 27 focused on the time of IACS' first lasing.

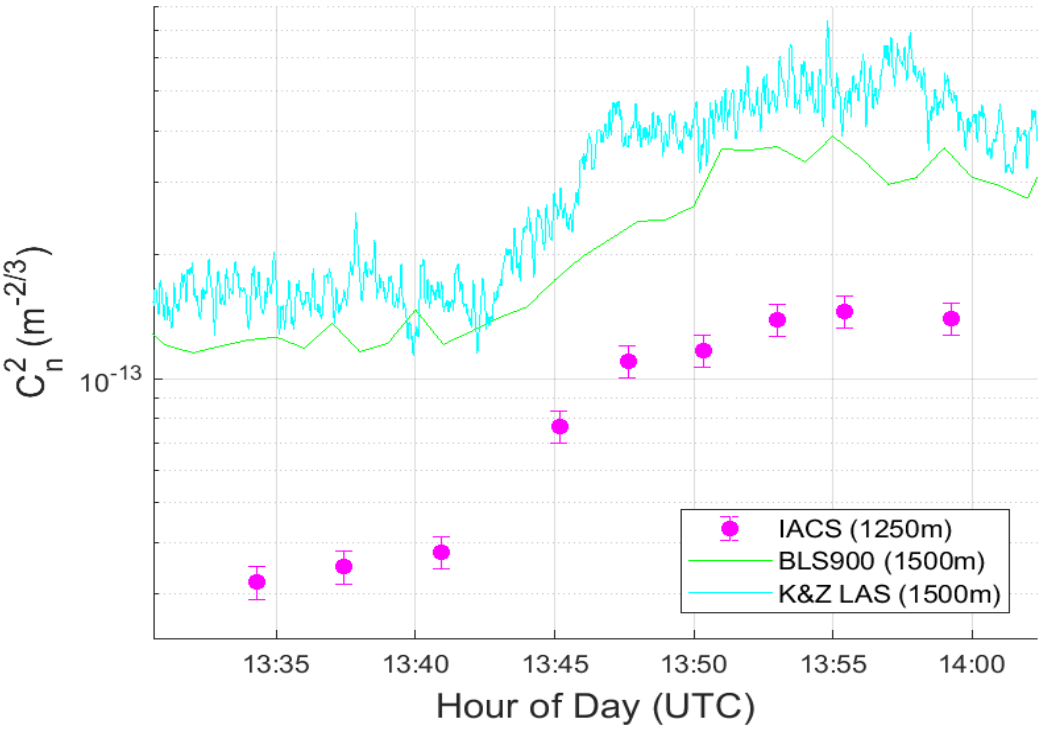

Figure 5.19: Path-averaged C_n^2 on June 27 focused on the time of IACS' second lasing.

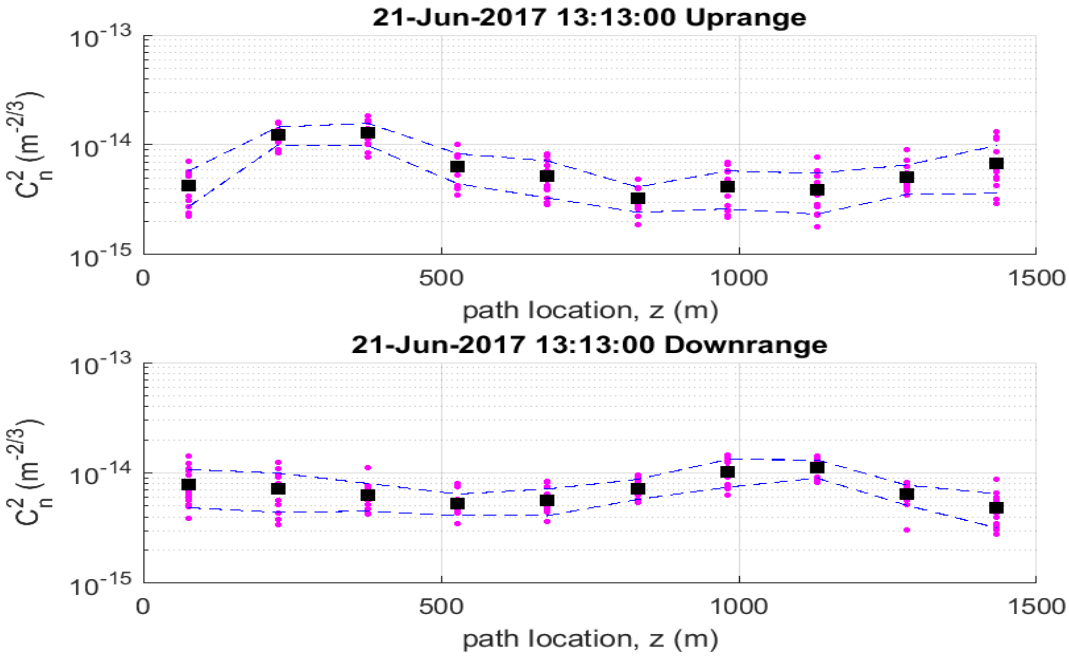

Figure 5.20: Comparison of path-weighted C_n^2 for DELTA uprange and downrange systems.

5.2 DELTA, PROPS and IACS path-profile results

The primary concern for the DELTA system is how its path-weighting functions apply zero-weight to turbulence measured at the target, where the average turbulence measure is strongest. This was accounted for at the data collection by placing two DELTA units next to each other at opposite orientations, labeled "uprange" and "downrange," previously shown in Figure 4.5. Section 5.1 shows that their path-averaged measurements mostly agree, sometimes diverging for a short duration, as expected. Figure 5.20 shows an example of path-specific measurements for a single time. 150 measurements (15 measurements at each of 10 range bins) per DELTA system are shown along with their mean (the black dot) and variance (the blue dotted lines). The mean of these 10 means is taken to be the path-averaged measurement at that time, which has constituted a single point on the plots shown in Chapter 5.1.

The zero-distance for the downrange system is the 1.5km distance of the uprange sys-

tem. Though the systems are pointed in opposite directions, their C_n^2 estimates follow the same trends, owing to the path-weighting functions used to estimate C_n^2.

PROPS also estimates turbulence across the path, but there is reason to doubt its accuracy with these measurements. Figure 5.21 shows PROPS', DELTA, and IACS measurements taken in the same minute. This is the only minute of the entire test in which data from all 4 systems was simultaneously captured. Also added is a "DELTA avg" line that is simply the average of the two DELTA results. PROPS' estimates are largely flat across the path due to its ability to harness many unique path-weighting functions. It rests along 10^{-13} across the path, while the DELTA units showed stronger changes. Figure 5.10 shows IACS 1250m agreeing with PROPS and DELTA down, while DELTA up reports a much lower measurement. Figure 5.21 shows that DELTA up measured weaker turbulence at the beginning of the path, and these measurements were given greater weight than the stronger measurements taken at the end of the path.

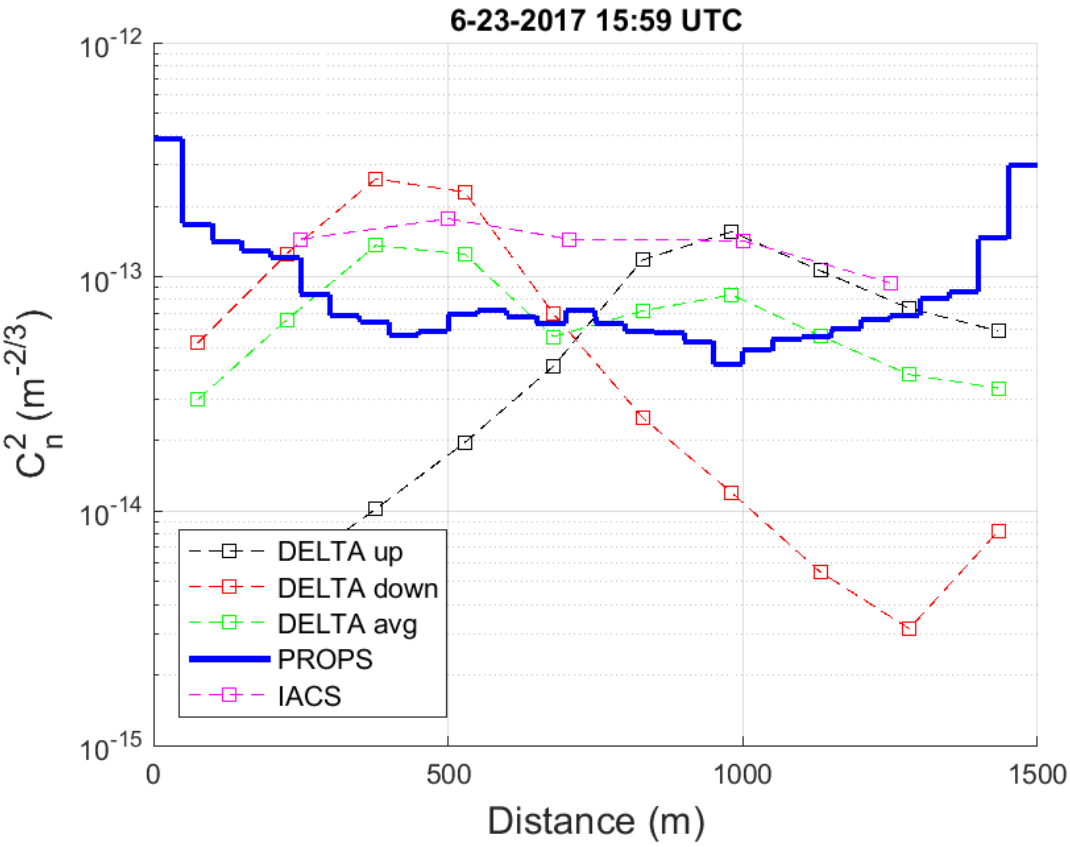

Figure 5.21: Same-minute path-averaged C_n^2 comparison of DELTA up, DELTA down, PROPS, and IACS.

CHAPTER 6
DISCUSSION

Given the many methods for measuring C_n^2, the focus of this thesis is to compare and contrast the efficacy of these different measurement methods. The trade space of these systems and techniques is evaluated, data reliability is addressed, opportunities for expansion are presented, and the thesis is concluded.

6.1 System Comparison and Evaluation

This section presents the trade space comparison between DELTA, PROPS, IACS, and scintillometers. Though other systems such as radar systems, SODAR systems, and balloons were introduced in Chapter 2, the four systems analyzed in this thesis demonstrate the differences and characteristics of DIM lidar, DDTV, and scintillometers. The other systems not mentioned here either measure something tangential to C_n^2 yet still interesting to atmospheric optics (such as the other two lidar subsystems on IACS) or require specialized hardware such that direct comparison with these four systems is less meaningful.

6.1.1 C_n^2 Measurements

The comparison plots from Chapter 5.1 show IACS OTP comparing favorably with the two DELTA systems, PROPS, and the scintillometers. IACS OTP measurements matched the magnitude of the two phase-based systems while tracking the trends of the irradiance-based scintillometers. DELTA path-averaged measurements between the uprange and downrange systems sometimes sharply differ at single-time measurements, despite their general agreement. This is discussed in greater detail below. PROPS path-averaged results matched well with DELTA, but its path-dependent measurements do not agree. The PROPS team identified an issue with the red LED source which skewed the measurements and path-

weighting functions of the system. The scintillometers consistently measured stronger turbulence than the phase-based systems. They mostly agreed with each other, though the K&Z measured much lower C_n^2 on June 26 prior to the rise to the unstable period as seen in Figure 5.14. One primary reason the scintillometers differ from the phase-based systems is that they measure scintillations, an irradiance-based phenomenon, as described in Chapter 2.3. Other differences with the phase-based systems include height above the ground of the transmitter and receiver and location, as the K&Z was next to IACS and the BLS-900 was placed alongside other equipment at the range. Differences in magnitude are common among scintillometers, so matching the trend over time is more important than exactly matching the magnitude of measured C_n^2.

The systems handle path-weighting of the C_n^2 profile differently, as described in Chapter 3. Scintillometers are weighted in the middle and pick up almost no turbulence effects at the source and receiver. DELTA picks up fluctuations from the receiver to halfway along the path, but has zero weighting at the target. Having the two DELTA units opposite each other and combining their results was an effort to address this path-weighting limitation. PROPS maintains resolution and sensitivity along the path, and applies unique weighting functions based on changing wavefront measurements. IACS uses a measurement weighting function that takes on a flatter shape primarily to maintain stability during the matrix inversion process, rather than a path-weighting function. Original DIM lidar path-weighting is focused nearer to the aperture, and DIM variance and error bounds increase as path length (and thus turbulence strength) increases. In terms of path-weighting, PROPS is the most comprehensive as it incorporates multiple unique functions all across the path. DELTA, IACS OTP, and scintillometers lose some C_n^2 information along the path as a consequence of the fundamental phenomena they utilize.

Table 6.1 summarizes the ratio differences between IACS and the other devices. Each row represents a grouping of similar IACS measurement runs, a set of measurements featured in the zoomed in Figures of Chapter 5. The Phase-based column represents the two

Row	K&Z	BLS-900	Phase-based	Day
1	N/A	4-6x	2x	23
2	N/A	2-3x	2-3x	24
3	N/A	2-3x	1x	24
4	N/A	2-5-10x	N/A	24
5	2x*	5x*	-2x*	26
6	5x	5x	2x	26
7	2-3x	2-3x	N/A	27
8	1x	2x	N/A	27
9	3-4x	2-3x	N/A	27

Table 6.1: Summary of C_n^2 measurement ratios relative to IACS.

DELTA units and PROPS, as measurements for all those systems were close enough together relative to an IACS measurement. The asterisked row consists of the discarded measurements taken on June 26th when the field of view of OTP was changed. IACS tracks the other phase-based systems around a factor of 2x. The largest disparity in measurement occurs between IACS and DELTA up on June 23rd (Figure 5.10) at 16:00 when DELTA down is coming back online after being down for a significant chunk of time. Barring this possibly egregious data point, IACS is as accurate as commercial phase-based path-profiling systems. IACS stays within 2-3x of the BLS-900 except for 3 measurements. Row 4 of Table 6.1 contains the drop covered in detail in Chapter 5.1.6. Rows 1 and 6 contain data recorded from 15:00-16:00 UTC on June 23rd and 26th. Figure 5.3 shows turbulence strength was reasonably high at this time for every day of BLS-900 measurements. This could be scintillometer saturation as this is 12:00-13:00 local time. Thus IACS agrees within 2-3x of the BLS-900 barring two different situations,rapid drops in C_n^2 intensity and strong afternoon turbulence. IACS less consistently agrees with the K&Z LAS. The K&Z had serious setup issues throughout the test, had much higher resolution, and was right next to IACS. K&Z captured the stable-unstable drop-jump more finely than the BLS-900, causing it to agree more with IACS during early morning measurements and resulting in the 1x agreement seen in Row 8 and Figure 5.18. Finally, could knowledge of the error

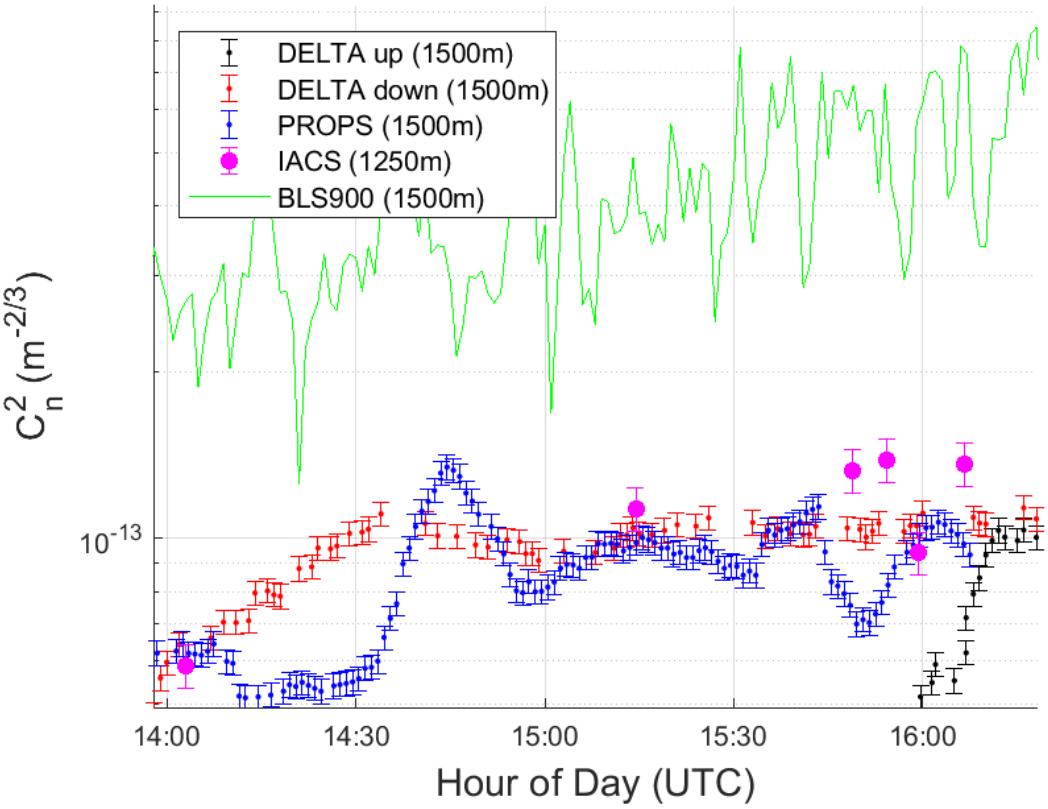

Figure 6.1: June 23rd zoomed-in with estimated error added.

bars on the instruments provide more insight? The mean relative error of the original prototype PROPS system is 5% [31]. It is unknown if this is still the error with the modern PROPS system. There are no publications for the DELTA system, but its fundamentals are the same as PROPS, so the 5% error bar can be applied to its measurements as well. Figure 6.1 shows Figure 5.10 but now with the potential 5% error bars. The DELTA down and PROPS error bars overlap for three of the six IACS measurements on June 23rd. Points only overlap for the closest data points anyway, so adding the estimated error bars does not offer new insight.

The DELTA units were oriented in opposite directions to utilize their path-weighting function to gain insight into how turbulence developed along the path over time, shown in Chapter 5.2. Each bin of the DELTA unit weights measurements closest to the receiver. Thus the uprange DELTA unit will overvalue turbulence measurements closer to the offi-

cial zero-point of the path, while the downrange DELTA unit will overestimate turbulence near the 1500m point. This gives three zones of comparison: up>down, up==down, and up<down. With up>down, we can assume that turbulence is stronger along the first half of the path. up==down gives confidence that turbulence is evenly distributed on the ends and weaker in the middle. up<down shows that turbulence is concentrated near the end of the path. Figure 5.12 demonstrates these zones and their occurrence over a 2-hour period. Based on the differential between up and down, it seems turbulence strength concentration moves along the range toward the receiver of the uprange unit, remains slightly concentrated there at 12:30, then moves back downrange and remains concentrated downrange from about 12:45 to 13:15, where the same trend repeats until about 14:15 when the devices again agree on magnitude. Wind and temperature data collected specifically along the path could give clues to the veracity of this claim. For instance, if wind velocity was oriented along the path toward the receiver then it would make sense for turbulence strength to push toward the downrange unit. One problem with using these measurements to elucidate this theory is our lack of insight into the errorbars of each DELTA measurement. If the measurement differential is within the errorbars of the measurements, then the path-weighting functions have less of an impact on measurement truth.

6.1.2 System Advantages vs. System Requirements

Figure 6.2 (briefly introduced in Chapter 3) summarizes system performance and technique advantages. The scintillometer, DELTA, and PROPS are transmitter receiver pairs or at least require a target to function properly. As discussed in Chapter 3.1, scintillometers must be properly aligned via rotations of the receiver telescope. Similarly, the PROPS system had to focus the separate LED arrays into each telescope aperture. The DELTA system is the most flexible. Although a high-contrast, specially-designed target board was used for CABLE-TRAX to get the best results, any suitable high-contrast scene with sufficient features could be imaged in place of a target board. Such scenes are often difficult to

Equipment and Basis	Measured phenomenon	Measurement technique	Advantages	Disadvantages
Scintillometer (K&Z and BLS-900) Basis: Irradiance Path-Profile: No	Scintillations - intensity fluctuations of a beam of light	Variance of fluctuations used to directly calculate Cn2	Direct measurement, long-established and verified, cheap and dependable	Probabalistic nature of scintillations, saturation at high turbulence, saturation at long distances (4.5km K&Z), double-ended
PROPS, Difference of Differential-Tilt Variance (DDTV) Basis: Phase Path Profile: Yes	Measures DTVs or tilt covariances from wavefronts of a source across a path, which are converted to weighted integrals of Cn2	Known weighted integrals of Cn2 and compared against the DTV measurements, then DTV's are inverted to produce Cn2 estimate	Can detect changes in turbulence along path resulting from the surface features along path, estimates cross-wind speeds as seen from both sides of path.	Double-ended, requires constant monitoring since two units must communicate results
DELTA, modified DDTV Basis: Phase Path Profile: Yes	Computer measures the differential jitter of feature pairs as a function of angular separation	Image processing techniques used to estimate Cn2 from jitter	Semi-single ended with appropriate high-contrast scene, immune to many sources of error, easy to deploy	Less accurate than PROPS
IACS, Differential Image Motion (DIM) lidar Basis: Phase Path-Profile: Yes	Centroid of artificial star determined in each aperture, and image variances of each centroid are captured for each aperture	Total variance of these separate centroid variances is measured and used to directly calculate r0	Truly single-ended, eliminates sources of error by using multiple apertures and source beams, slant-path measurements possible	Large, difficult to deploy and operate, expensive, LCH required for vertical measurements

Figure 6.2: Summary Comparison of devices presented.

come across, but Figure 6.3 shows some demonstrative examples [38]. IACS OTP is the only system that is not bound by this target restriction and can be considered single-ended. DIM lidar in general and thus IACS OTP opens up new possibilities for measuring the atmosphere of less cooperative environments, such as across the open sea or along the coast (i.e. littoral zone). These environments were previously inaccessible to double-ended measurement systems due to difficult measurement conditions such as a varying surface. Since IACS does not require a target or other transceiver, it can measure C_n^2 along such a path.

IACS OTP's benefit of single-ended measurements comes with IACS' detriment: its large size and operational requirements. Firing a lidar into the air requires strict windows dictated by the Laser Clearing House and administered in cooperation with the nearest Air Traffic Control tower, which will safely redirect all flights away from the laser. This is in strong contrast to DELTA, which trends towards reducing all components to simply a computer and a camera-telescope package.

This emphasis on ease of use extends to ease of setup. DELTA is by far the easiest sys-

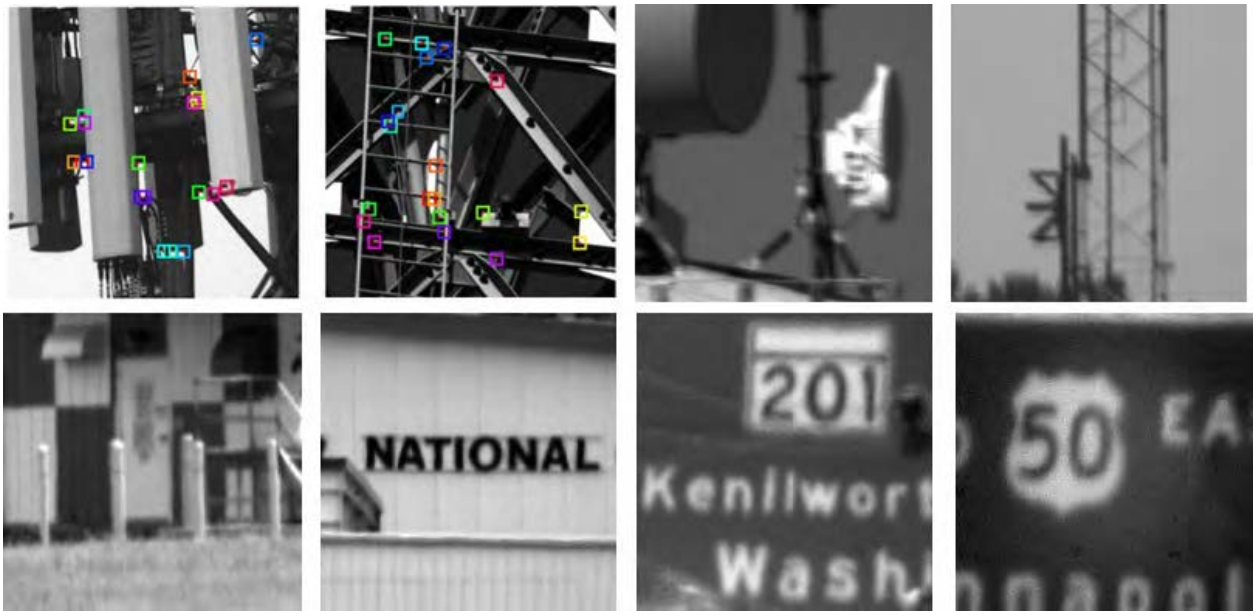

Figure 6.3: Potential targets-of-opportunity for a DELTA system to image and measure turbulence across [38].

tem to setup: point the camera at a scene (or target board) and start taking measurements and processing data on the computer. PROPS and scintillometers require fine-tuned alignment, as previously mentioned. IACS currently requires over an hour of warmup prior to operation, involving a manual and error-prone laser tuning process. The strength of laser-power developed during this process affects the efficacy of resultant measurements, since more laser power directly results in brighter guidestars and higher signal-to-noise ratio. DELTA, PROPS, and scintillometers do not require a laser tuning process and have simpler setup procedures.

In keeping with simplicity of components is the portability of the systems. DELTA, PROPS, and scintillometers have a smaller footprint for transportation. Two scintillometers with two telescoping tripods, a battery for the receiver unit, and power and data cables for the transmitter unit, can fit into the back of a truck. PROPS is similarly suited, while a single DELTA setup can fit into the trunk of a car. IACS is portable, but requires a crane and a tractor trailer for movement. This again demonstrates the portability and versatility of PROPS, DELTA, and the K&Z LAS, though it is important to note that these are

production-ready systems, while IACS is an experimental prototype.

6.2 Reliability of Results

The truth of C_n^2 is defined by its expected statistical performance which follows the turbulence structure function $D_n(R)$. Kolmogorov's structure function is valid within the inertial subrange. Von Karman's structure function incorporates inner and outer scale and is accurate outside the inertial subrange [9]. Each system had challenges with data collection. The PROPS team faced issues aligning the downrange terminal, and could not immediately address it due to range logistics for safety while IACS was operating. A problem was discovered after observing that the red LED was not focused correctly when compared to the green and blue LEDs. This mismeasurement propagated throughout the weighting functions described in Chapter 3.2 and subsequent measurements. The issue is not observed in path-averaged results, but brings weighted-path results for the PROPS system into question. IACS 250m measurements suffered from a resonance that compromised almost all the measurements. They appear aberrant in almost every test when compared to the other IACS range measurements along the path during the same measurement period, which will be investigated further. K&Z Scintillometer data was unavailable for multiple days of the test because of integration issues.

6.3 Future Work

The final day of testing involved taking IACS measurements along a varying path. The idea is that single-ended lidar measurements can be used determine different "slabs" or surface types along a path. The forward model (Equation 3.14) can be split up linearly so that

$$\sigma_{DIM}^2 = AC_{n1}^2 \int_0^{h_0} (1 - h/h_0)^{5/3} dh + AC_{n2}^2 \int_{h_0}^{H} (1 - h/H)^{5/3} dh, \tag{6.1}$$

where A is a constant found using the subaperture parameters D and d and C_{n1}^2 and C_{n2}^2 are two different C_n^2 values for the two different slabs. h_0 is the point at which the slabs change surface type. This point should be able to be determined solely from data collected. Since DIM variance measurements should monotonically increase, two different slopes of DIM variance measurements should be detected for two slabs. Thus a linear regression can be performed on the measurement data, and the intersection of the two trends of DIM variance should reveal h_0. With h_0, the integrals can be solved for a constant value and the equations inverted to produce two C_n^2 trend lines based on the two DIM variance trend lines. Unfortunately, many of the runs on June 28th lacked monotonically increasing data. A test plan designed to verify this functionality for 2 or more slab types would verify the best regression technique and the limits of this capability. The ability to determine slabs would be of particular use at the littoral zone, where a path could consist of asphalt, grass, sand, and roiling water. There may even be differently-surfaced slabs of an all-water path that each deserve a separate C_n^2 value.

6.4 Opportunities for future testing

The CABLE-TRAX test plan and execution has room for improvements for future measurements. Given the size and diversity of the teams involved, the test director chose to employ a largely hands-off approach, except for enforcement of laser safety protocol. Advantages to this style of test organization include maximum data acquisition and operational freedom of teams. The biggest disadvantage is fewer second-by-second comparison options. One important act of data quality taken near the beginning of the test was to sync most equipment to a specific UTC time. Additional disruptions came from IACS lasing, preventing many teams from fixing their downrange equipment. A second test to more accurately compare these systems and fully verify IACS would benefit from a test plan that incorporates these changes:

1. Place all equipment as close together as possible and at the same height. IACS

measured the turbulence of air some feet higher off the ground than the other pieces of equipment.

2. To properly compare against what IACS does, walk out the second part of the other pieces of equipment at 250, 500, 750 m, etc. This would be time consuming or could be accomplished with multiple sets of equipment. In this way, each of IACS' range bins could be tested/validated with a slew of other equipment rather than just its longest range bin. This other equipment should include sun photometers to track cloud coverage and sonic anemometers to track wind velocity and estimate C_V^2. This could also help IACS with determining more subtle sources of error similar to the ringing observed at some short range measurements.

3. Determine a variant-path baseline. Scintillometers are less ideal for this because they will simply average the result. Some other piece of equipment/technique/simulation result would be needed. Using the grass-runway testing as an example, two sets of scintillometers could be set up, one set over grass and the other set over runway. Then the IACS slabbing technique could be compared to the separate results of the scintillometers. This would be simpler to test than the previous experiment because IACS OTP could build a range profile through its standard operation.

6.5 Conclusion

IACS OTP measurements matched the magnitude of the two phase-based systems while tracking the trends of the irradiance-based scintillometers. Its single-ended operation enables it to build path-profiles along non-cooperative paths that have as yet escaped profiling. Given that IACS is a prototype, decreasing its SWaP and cost would lead it to a supporting role in directed energy and other atmospheric characterization applications. If one measures across a more accessible path than the littoral zone or if laser safety is a concern, DELTA provides production-ready semi-single-ended C_n^2 measurements today. Even though there were problems with the data collection for PROPS, this system offers comprehensive path-

profiling for any path in which a double-ended system suffices. Scintillometers continue to serve as the baseline to compare new measurement techniques against. In conclusion, this thesis met its research objective. Turbulence measurement systems were compared from fundamental physics all the way to measurement results and system utility. The experimental results of this thesis will influence further work in a wave optics simulation incorporating the C_n^2 values measured.

REFERENCES

[1] G. G. Gimmestad, M. W. Dawsey, D. W. Roberts, J. M. Stewart, J. W. Wood, F. D. Eaton, M. L. Jensen, and R. J. Welch, "Field validation of optical turbulence lidar technique," *Proc. SPIE*, vol. 5793, no. Atmospheric Propagation II, 2005.

[2] F. D. Eaton, "Recent developments of optical turbulence measurement techniques (invited paper)," *Proc. SPIE*, vol. 5793, no. Atmospheric Propagation II, 2005.

[3] A. N. Kolmogorov, "The local structure of turbulence in incompressible viscous fluid for very large reynolds numbers," *Proceedings: Mathematical and Physical Sciences*, vol. 434, no. 1890, pp. 9–13, 1941.

[4] A. M. Obukhov, "Structure of the temperature field in turbulent flow," *Izvestiia Akademii Nauk S.S.S.R., Ser. Geogr. i Geofiz.*, vol. 13, pp. 58–69, 1949.

[5] S. Corrsin, "On the spectrum of isotropic temperature fluctuations in an isotropic turbulence," *Journal of Applied Physics*, vol. 22, no. 4, pp. 469–473, 1951.

[6] D. L. Fried, "Statistics of a geometric representation of wavefront distortion," *Journal of the Optical Society of America*, vol. 55, no. 11, pp. 1427–1435, 1965.

[7] V. I. Tatarskii, *The Effects of the Turbulent Atmosphere on Wave Propagation*. Jerusalem, Israel: Israel Program for Scientific Translations, 1971.

[8] A. Ishimaru, *Wave Propagation and Scattering in Random Media*. New York, NY: Academic Press, 1978.

[9] L. C. Andrews and R. L. Phillips, *Laser Beam Propagation through Random Media, Second Edition*. Bellingham, WA: SPIE Press, 2005.

[10] R. C. Hardie, J. D. Power, D. A. LeMaster, D. R. Droege, S. Gladysz, and S. Bose-Pillai, "Simulation of anisoplanatic imaging through optical turbulence using numerical wave propagation with new validation analysis," *Optical Engineering*, vol. 56, pp. 56 –56 –16, 2017.

[11] J. D. Schmidt, *Numerical Simulation of Optical Wave Propagation with Examples in Matlab*. Bellingham, WA: SPIE Press, 2010.

[12] S. F. Clifford, "The classical theory of wave propagation in a turbulent medium," in *Laser Beam Propagation in the Atmosphere*, J. W. Strohbehn, Ed. Berlin, Heidelberg: Springer Berlin Heidelberg, 1978, pp. 9–43, ISBN: 978-3-540-35826-8.

[13] J. C. Owens, "Optical refractive index of air: Dependence on pressure, temperature and composition," *Applied Optics*, vol. 6, no. 1, pp. 51–59, 1967.

[14] R. R. Beland, "Propagation through atmospheric optical turbulence," in *The Infrared and Electro-Optical Systems Handbook. Atmospheric Propagation of Radiation, Volume 2*, F. G. Smith, Ed. Environmental Research Institute of Michigan, Jan. 1993, pp. 157–232.

[15] R. S. Lawrence, G. R. Ochs, and S. F. Clifford, "Measurements of atmospheric turbulence relevant to optical propagation," *Journal of the Optical Society of America*, vol. 60, no. 6, pp. 826–830, 1970.

[16] Training and Education Services Branch, *Aviation Routine Weather Report*, `http://meteocentre.com/doc/metar.html`, Accessed: 2018-10-04.

[17] S. F. Clifford, G. R. Ochs, and R. S. Lawrence, "Saturation of optical scintillation by strong turbulence," *Journal of the Optical Society of America*, vol. 64, no. 2, pp. 148–154, 1974.

[18] T.-i. Wang, G. R. Ochs, and S. F. Clifford, "A saturation-resistant optical scintillometer to measure cn2," *Journal of the Optical Society of America*, vol. 68, no. 3, pp. 334–338, 1978.

[19] G. G. Gimmestad, D. W. Roberts, J. M. Stewart, and J. W. Wood, "Development of a lidar technique for profiling optical turbulence," *Optical Engineering*, vol. 51, no. 10, 2012.

[20] M. Sarazin and F. Roddier, "The eso differential image motion monitor," *Astronomy and Astrophysics*, vol. 227, pp. 294–300, 1990.

[21] F. D. Eaton, S. A. McLaughlin, and J. R. Hines, "A new frequency-modulated continuous wave radar for studying planetary boundary layer morphology," *Radio Science*, vol. 30, no. 1, pp. 75–88, 1995.

[22] G. D. Nastrom and F. D. Eaton, "Turbulence eddy dissipation rates from radar observations at 520 km at white sands missile range, new mexico," *Journal of Geophysical Research: Atmospheres*, vol. 102, no. D16, pp. 19 495–19 505, 1997.

[23] ——, "Persistent layers of enhanced cn2 in the lower stratosphere from vhf radar observations," *Radio Science*, vol. 36, no. 1, pp. 137–149, 2001.

[24] ——, "The coupling of gravity waves and turbulence at white sands, new mexico, from vhf radar observations," *Journal of Applied Meteorology*, vol. 32, pp. 81–87, 1993.

[25] F. F. Forbes, E. S. Barker, K. R. Peterman, D. D. Cudaback, and D. A. Morse, "High altitude acoustic soundings," in *1985 Technical Symposium East*, vol. 0551, SPIE, p. 14.

[26] F. D. Eaton, P. R. Kelly, D. T. Kyrazis, and S. S. Stokes, "Refractivity turbulence observations using a new balloon-ring platform," in *AeroSense 2002*, vol. 4724, SPIE, p. 7.

[27] F. D. Eaton, B. B. Balsley, R. G. Frehlich, R. J. Hugo, M. L. Jensen, and K. A. McCrae, "Turbulence observations over a desert basin using a kite/tethered-blimp platform," *Optical Engineering*, vol. 39, p. 10, 2000.

[28] M. R. Whiteley, "Rytov parameter estimation by use of differential-tilt measurements," in *International Symposium on Optical Science and Technology*, vol. 4125, SPIE, 2000, p. 14.

[29] H. A. R. De Bruin, B. J.J. M. Van Den Hurk, and W. Kohsiek, "The scintillation method tested over a dry vineyard area," *Boundary-Layer Meteorology*, vol. 76, no. 1, pp. 25–40, 1995.

[30] Kipp and Zonen, "Las and x-las instruction manual," Kipp and Zonen, Manual, 2007.

[31] M. R. Whiteley, D. C. Washburn, and L. A. Wright, "Differential-tilt technique for saturation-resistant profiling of atmospheric turbulence," in *International Symposium on Optical Science and Technology*, vol. 4494, SPIE, 2002, p. 12.

[32] D. W. Roberts, K. R. Albers, E. A. Brown, T. A. Craney, M. M. Hosain, R. K. James, N. D. Meraz, A. J. Mercer, K. D. Nielson, R. L. Ortman, T. W. Pool, J. W. Wood, J. M. Stewart, T. M. Strike, G. G. Gimmestad, and D. N. Whiteman, "The integrated atmospheric characterization system (iacs)," *Proc. SPIE*, vol. 9080, no. Laser Radar Technology and Applications XIX; and Atmospheric Propagation XI, 2014.

[33] F. D. Eaton, W. A. Peterson, J. R. Hines, J. J. Drexler, A. H. Waldie, and D. B. Soules, "Comparison of two techniques for determining atmospheric seeing," *Proc. SPIE*, vol. 0926, no. 1988 Technical Symposium on Optics, Electro-Optics, and Sensors, p. 16,

[34] M. S. Belenkii, D. W. Roberts, J. M. Stewart, G. G. Gimmestad, and W. R. Dagle, "Experimental validation of the differential image motion lidar concept," *Optics Letters*, vol. 25, no. 8, pp. 518–520, 2000.

[35] M. S. Belen'kii, D. W. Roberts, J. M. Stewart, G. G. Gimmestad, and W. R. Dagle, "Experimental validation of the differential image motion lidar concept," *Proc. SPIE*, vol. 4377, no. Aerospace Defense Sensing, Simulation, and Controls, p. 10, 2001.

[36] C. Fernandez and G. Bennett, "Comparison of measurement techniques used to determine atmospheric structure parameter," in *Imaging and Applied Optics 2018 (3D, AO, AIO, COSI, DH, IS, LACSEA, LS&C, MATH, pcAOP)*, Optical Society of America, 2018, JW5I.2.

[37] S. Hammel and K. McBryde, "Cable-trax test plan," SPAWAR, Test Plan, 2017.

[38] M. A. Corporation, "Imaging path atmospheric turbulence monitor pm-02-600 users manual," MZA, Manual, 2017.